Global and Planetary Change 199 (2021) 103434

Contents lists available at ScienceDirect

Global and Planetary Change

journal homepage: www.elsevier.com/locate/gloplacha

Evolution of deformation mechanism and fluid flow in two pre-rift siliciclastic deposits (Pannonian Basin, Hungary)

Barbara Beke [a,*], Emese Szőcs [a], Kinga Hips [a], Félix Schubert [b], Attila Petrik [c], Rastislav Milovský [d], László Fodor [a,e]

[a] MTA-ELTE Geological, Geophysical and Space Science Research Group, Pázmány P. sétány 1/C, 1117 Budapest, Hungary
[b] Department of Mineralogy, Geochemistry and Petrology, University of Szeged, Egyetem utca 2-6, 6702 Szeged, Hungary
[c] Eriksfiord AS, Prof. Olav Hanssensvei 7A, 4021 Stavanger, Norway
[d] Slovak Academy of Sciences, Earth Science Institute, Ďumbierska 1, SK-974 01 Banská Bystrica, Slovakia
[e] Eötvös Loránd University, Department of Physical and Applied Geology, Pázmány P. sétány 1/C, 1117 Budapest, Hungary

ARTICLE INFO

Keywords:
Deformation band
Calcite cementation
Stable isotope
Burial history
Fluid flow
Fluid composition

ABSTRACT

Distinct stages of deformation and fluid flow-related diagenetic alterations are recorded in Lower Miocene sandstone and conglomerate of the Pannonian Basin, Central Europe. Multiple generations of structural elements (deformation bands, calcite dominoes and veins) as well as host rocks were investigated using petrographical, elemental and stable isotope geochemical methods together with fluid inclusion petrography and microthermometry. The integration of acquired structural and diagenetic data into a subsidence model constrains the spatial and temporal evolution of deformation mechanisms and diagenetic processes. The six investigated sites represent central and marginal areas during both the pre-rift and *syn*-rift phases of basin evolution. The elements of pre-rift phases were preserved at the eastern margin, where eogenetic calcite precipitated in the host rocks and in the early types of deformation bands. Their δ^{18}OPDB isotope values from −4.3‰ to −1.9‰ paired with $\delta^{13}C_{PDB}$ isotope values from −3.8‰ to 1.8‰ refer to precipitation from connate marine and mixed marine and meteoric pore water. The *syn*-rift phases are represented by eogenetic calcite and start of shallow mesogenetic diagenetic alterations in marginal position as well as in the basin centre. The δ^{18}OPDB and $\delta^{13}C_{PDB}$ isotope ratios in these calcites yielded values from −15.2‰ to −5.7‰ and from to −18.5‰ to -–1.6‰, respectively. The gradual depletion in heavy isotopes shows positive covariance as the deformation progressed in time. This trend is attributed to an increasing proportion of deeply circulating meteoric fluid. The sporadic fluid inclusion data confirm meteoric fluid contribution to certain carbonate cement phases. The distinguished calcite generations in pre-rift and *syn*-rift structural elements and host rocks were mainly related to the phases of intense subsidence that, together with the increased rift-related heat flow, warmed up the circulating fluids. The isotope values deviating from the general trend allow the recognition of local source of light carbon contribution to basin-wide fluid-flow evolution, and cannot be tied to the switch in tectonic settings from pre-rift compression to *syn*-rift extension.

1. Introduction

Deformation and diagenesis are closely linked processes during the evolution of siliciclastic sedimentary basins (e.g. Knipe, 1993; Laubach et al., 2010). Deformation in porous siliciclastic deposits starts with the development of deformation bands (DB; after Aydin, 1978). These bands are tabular, fault-like structures along which offsets of millimetre to tens of centimetres take place without a macroscopic discontinuity surface. Deformation bands can be formed by various mechanisms (Fossen et al., 2007), where petrophysical properties of the host rocks, pressure, temperature and tectonic regime are the most significant control factors (Schultz and Siddharthan, 2005; Ballas et al., 2014; Soliva et al., 2016). During progressive burial as rheology of the rocks changes during diagenesis the deformation progresses from grain reorganization without fracturing toward increasing proportion of grain breakage (cataclasis) accompanied by increasingly reduced porosity (Fossen et al., 2007). A possible scenario of decreasing porosity is the end of DB evolution when the mechanism switches to frictional slip along a discrete

* Corresponding author.
E-mail address: barbara.beke@gmail.com (B. Beke).

https://doi.org/10.1016/j.gloplacha.2021.103434
Received 15 May 2020; Received in revised form 15 January 2021; Accepted 27 January 2021
Available online 2 February 2021

fault planes or leads to extension fractures, or veins (Aydin and Johnson, 1978).

Therefore, the deformation mechanisms and diagenetic alterations are closely interconnected. In this interaction, the consolidation and lithification of the deposits determine the style of failure, while the type of actively forming structural element influence the possible fluid flow path. Many studies have investigated temporal evolution of paleo-fluid flow composition through observations of associated diagenetic alteration and cementation along faults (e.g. Travé et al., 1998; Chan et al., 2000; Boles et al., 2004; Beitler et al., 2005; Hodson et al., 2016; Andre et al., 2010; De Boever et al., 2011; Beaudoin et al., 2014; Ogata et al., 2014; Williams et al., 2017). In initially porous siliciclastic rocks, carbonate concretions associated with deformation structures are widely used as indicators of paleo-fluid flow (e.g. Mozley and Goodwin, 1995; Eichhubl et al., 2004, 2009; Milliken et al., 2009; Balsamo et al., 2012).

Although, deformation bands (DB) are ubiquitous structures in poorly lithified sediments, they were used for detailed diagenetic investigations only in limited cases (e.g. Eichhubl et al., 2004; Hodson et al., 2016; Balsamo et al., 2012; Lommatzsch et al., 2015a, 2015b.; Beke et al., 2019). DBs can either behave as path (Balsamo et al., 2012; Beke et al., 2019) or barrier to fluid flow (Pittman, 1981; Antonellini and Aydin, 1994; Davatzes et al., 2003; Shipton et al., 2005; Torabi and Fossen, 2009; Ballas et al., 2012; Tueckmantel et al., 2012; Torabi et al., 2013; Rotevatn et al., 2013) depending on their deformation mechanism. Therefore, bands can change the pattern of fluid flow by their geometry due to the formation of large permeability contrast and thus high effective permeability along bands (Sigda et al., 1999; Rotevatn et al., 2013). Due to the various fluid-path modifying behaviours of deformation bands, and the fast and irreversible changes in their deformation mechanism, these structures can be sensitive depth indicators of diagenetic processes.

In the present study, calcite cements are investigated by structural, petrographical, fluid inclusion and geochemical methods in distinct types of deformation bands, veins and host rocks. The host siliciclastic successions, the Lower Miocene Pétervására Sandstone (PF) and its Darnó Conglomerate Member, deposited just prior to the main rifting phase of the Pannonian Basin (Fig. 1).

The main aims of this paper are to (1) define petrographical and isotope geochemical characteristics of cement generations associated with temporally well-constrained deformation elements of the two types of siliciclastic successions; (2) connect diagenetic alterations, mainly calcite precipitation, with possible temperature and depth conditions of deformation processes, (3) recognise local and regional trends in paleo fluid-flow properties, (4) determine the influence of structural style and deformation mechanism in fluid-flow evolution at burial conditions <1.5 km, (5) contribute to better understanding the interaction of deformation, fluid flow and diagenesis as important part of Miocene basin evolution in the Pannonian Basin.

2. Geological setting

2.1. The Pannonian Basin

The Pannonian Basin was formed by lithospheric stretching which affected the overthickened crust of the Alpine–Carpathian-Dinaridic orogeny (Horváth et al., 2015; Balázs et al., 2016). Prior to the formation of the Pannonian Basin, *syn-* to post-collisional deformation of this orogenic belt occurred in a series of retroarc flexural basins of Middle Eocene to earliest Miocene age (Báldi, 1986; Tari et al., 1993). The study area is part of the North Hungarian–South Slovakian Paleogene Basin (NHSSPB, Fig. 1A). The basin centre is marked by gentle folds with wavelength of ca. 100 km, whereas the basin margins was delineated by fault zones of pure reverse or oblique reverse–strike-slip character (Sztanó and Tari, 1993; Fodor et al., 1999, 2005; Palotai and Csontos, 2010). The investigated sandstone and conglomerate deposits represent the last phase of the basin fill deposited between ~22–18.5 Ma (Fig. 1B). During a short period of terrestrial denudation during ~18.5–18.2 Ma, the Lower Miocene sequence was exposed to the surface and was slightly deformed and eroded.

The studied rocks underwent significant syn-rift deformation and subsidence during the formation of the Pannonian Basin proper. Syn-rift sedimentation started around 18.2 Ma parallel with the formation of first rhyolitic volcaniclastic deposits (Lukács et al., 2018). Stratigraphic data (Hámor, 1985) indicate that syn-rift deformation and associated subsidence accelerated from 17.3 Ma and remained significant till 12.8 Ma (Karpatian and Badenian age, respectively, see recent chronological calibrations of Hohenegger et al., 2014; Sant et al., 2017; Kováč et al., 2018). Most of the Late Miocene (from ~9 Ma) represents the post-rift stage when faulting largely deminished and subsidence was controlled by lithospheric process (Balázs et al., 2016).

The studied Lower Miocene (Eggenburgian) Pétervására Formation is located in the eastern and central parts of the basin. The sediments were deposited in a tide-influenced shallow sea within the Carpathian arc (Sztanó and Tari, 1993; Sztanó, 1994, 1995). The cross-bedded glauconitic sandstone is predominant in the central part of this basin (Fig. 1C; Báldi, 1986; Vass et al., 1988), whereas conglomerate was deposited along the eastern shoreline in fan-deltas (Darnó Conglomerate Member). The studied sites located in the eastern part of the basin are distributed along the Darnó Fault, which is the main structure of the wider Darnó Zone (Fig. 1D,E; Zelenka et al., 1983; Fodor et al., 2005; Petrik et al., 2016). Along this zone, an intra-basinal high developed, where Paleogene–Early Miocene rocks are missing. The clastic components of sandstones and conglomerates were derived from this high are diverse igneous rock types (Kovács et al., 2010; Sztanó and Józsa, 1996). The age of the conglomerate is 21.21 + 0.21/−0.27 Ma defined by Sr isotope of bivalve shells (Less and Frijia, 2015). A previous diagenetic study revealed the presence of an early marine and a mesogenetic calcite cementation in the sandstone (Szőcs and Hips, 2018); these data will be complemented by new structural observations from additional localities.

2.2. Relevant deformation phases

The cenozoic deformation of the study area was subdivided into 10 brittle deformation phases (from D1 to D10; Petrik et al., 2016; Beke et al., 2019) but only the relevant information is summarized below (Fig. 1B). The deposition of the studied rocks occurred during the D2 and D3 phases, before the onset of rifting. Phase D2 was characterised by NW–SE compression and lasted from ~25 to 20.5 Ma and the oldest studied site M-Da was deposited during the late part of this phase. The subsequent D3 phase had transpressional character with roughly E–W trending compressional principal stress axis. It corresponds to major dextral strike-slip faulting along the southern boundary zone of the entire NHSSPB (Fig. 1A; Csontos and Nagymarosy, 1998). The D3 phase lasted through the end of the host sandstone deposition (~18.5 Ma) until the subsequent denudation and terrestrial sedimentation (18.2 Ma, Fig. 1B). The two pre-rift deformation phases reactivated the Darnó Zone as a sinistral-reverse and purely reverse fault (D2 and D3 phases, respectively; Sztanó and Tari, 1993; Sztanó and Józsa, 1996; Fodor et al., 2005; Kovács et al., 2020). These two contractional phases resulted in a few-km-wide thrust zone (Darnó zone) that contains the three basin margin sites.

The succeeding D4 phase already represents the onset of extensional deformation, when the rifting of the Pannonian Basin initiated (Fig. 1B). The D4, D5 and D6 phases are marked by extensional stress field whose minimal stress axis gradually rotated from NNE–SSW to ESE–WNW (Petrik et al., 2016) and the main normal fault directions changed accordingly. These extensional episodes are separated by two well-documented counterclockwise vertical-axis rotation (Márton and Fodor, 1995). The rotation events and volcanoclastic levels constraint the D5 phase between 17 and 15 Ma, when typical *syn*-rift grabens formed (e.g., Etes graben on Fig. 1A,C). Another set of grabens with

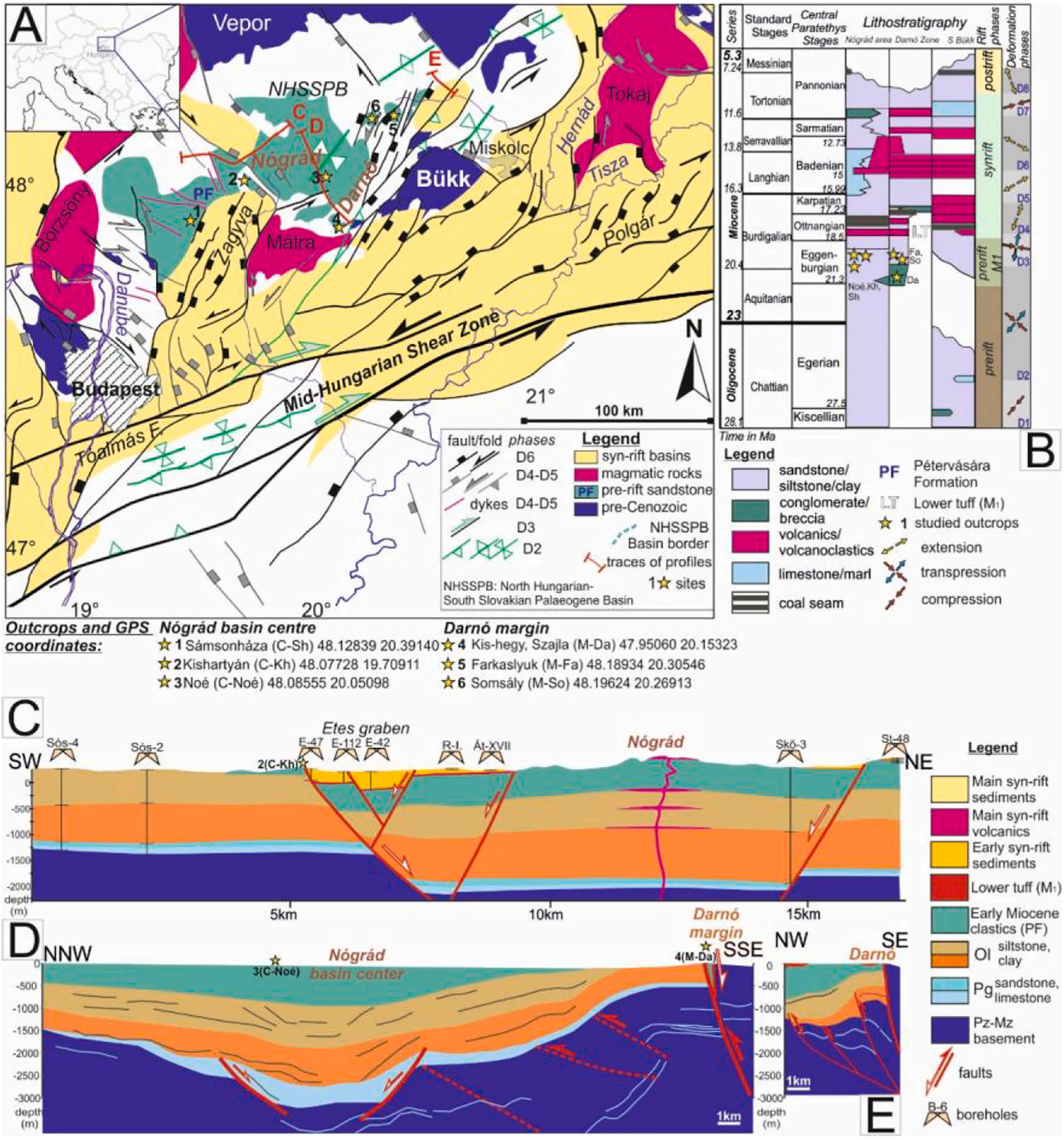

Fig. 1. A) Simplified geological setting of the area showing the main structures and outcrops. B) Stratigraphic column of study area with sampling points and tectonic phases. C) Geological cross-section along the SW-NE direction within the study area. D, E) Interpreted seismic sections (Ek-1 and So-2) along the NW-SE direction within the study area. A, B, C after Beke et al. (2019), and D, E after Kovács et al. (2020), both modified.

NNE–SSW strike formed during the D6 phase and the Darnó Zone was reactivated with normal kinematics. After a short ENE–WSW to E–W compression during the D7 phase, the D8 phase is characterised by (N) NW–(S)SE trending extension, which changed again to ESE–WNW extension during the D9 post-rift phase.

3. Methodology

3.1. Samples and methods

Samples were collected from five outcrops and one core section. Three of the six localities are along the Darnó Zone (the eastern margin of the basin), whereas the three others belong to the central part of the basin (Fig. 1, indicated by M- and C- prefixes, respectively). Samples were taken from host rocks and structural elements including deformation bands and calcite veins.

The thin sections were stained with Alizarin Red S and K-ferricyanide as described by Dickson (1966) in order to recognise and determine carbonate minerals. They were examined by conventional microscopic petrographical methods. The diagenetic crystal size was described according to Folk's (1974) classification. Cathodoluminescence (CL) studies were performed using a MAAS-Nuclide ELM-3 cold-cathode CL device on polished thin sections in order to reveal the characteristics of carbonate and authigenic albite. Cathodoluminescence images on veins were also obtained using a Reliotron VII CL instrument operating at 7 kV and 0.7 mA, mounted on an Olympus BX43 microscope.

Amray 1830i type Scanning Electron Microscope equipped with INCA Energy-dispersive X-ray spectrometer was used in secondary electron (SE), backscattered electron (BE) modes and Hitachi S-4700, 0.5–30 kV type Scanning Electron Microscope on polished thin sections and on broken surfaces. SEM microscopy was applied for a qualitatively more accurate mineral identification and revealing the microstructure of deformation bands.

The calcite phases of the host rock and the bands were analysed for their $\delta^{13}C_{PDB}$ and δ^{18}OPDB isotopic composition. Sampling of calcite phases was carried out with MicroMill. Samples were taken from bulk calcite cement of host rocks and from the core or marginal zone of deformation bands. Pulverized samples were reacted with H_3PO_4 at 70 °C under vacuum in autopreparation device Kiel IV following the method of (McRea, 1950), CO_2 gas was cryogenically purified and measure in dual-inlet mode on mass spectrometer MAT 253 (Thermo Scientific). Values are reported as permil vs. PDB and were calibrated using international reference material NBS18 and two working standards with $\delta^{13}C = 5.014‰$, $+2.48‰$, $-9.30‰$ and $\delta^{18}O = -23.2‰$, $-2.40‰$, $-15.30‰$, respectively. The typical precision of measurement is 0.02‰ for carbon and 0.04‰ for oxygen.

Microthermometry was carried out on a Linkam THMSG 600 heating-freezing stage mounted on an Olympus BX41 microscope equipped with 100× long-working-distance objective. Doubly polished 60- to 70 -μm-thick chips were first mapped for fluid inclusions. The instrument was calibrated using synthetic CO_2–H_2O fluid inclusions at −56.6 °C (T_mCO_2) and using pure H_2O inclusions at 0.0 °C (T_mIce) and at 374 °C ($T_h$critical). The microthermometric results reported below have accuracy of ±0.2 °C at $T < 100$ °C.

Burial history and isotherms are modelled by Petromod 1D software integrating borehole data, the thickness and lithology of the formations, postulated water depth and the calculation results of eroded thickness derived from cross sections; (Beke et al., 2019).

3.2. Concepts

A systematic change was demonstrated in deformation mechanisms within the pre- and *syn*-rift sediments in this part of the Pannonian Basin (Petrik et al., 2014; Beke et al., 2019). As predicted by theoretical considerations (Fossen et al., 2007), deformation mechanisms tend from disaggregation type deformation band to different stages of cataclastic type deformation bands (Petrik et al., 2014), then to the coexistence of DBs and extension veins, finally leading to the formation of discrete frictional slip along discrete fault planes, shear or hybrid-type joint, or extension veins without DBs (Beke et al., 2019). As the characteristic orientation of fractures and the governing stress field axes exhibit frequent and rapid changes (see 2.2.), the time constraints for different deformation mechanisms are quite exact.

The above described idealised chronological order of deformation structures was projected into 1D subsidence models to determine depth ranges for the formation of a given type of fracture (see Beke et al., 2019

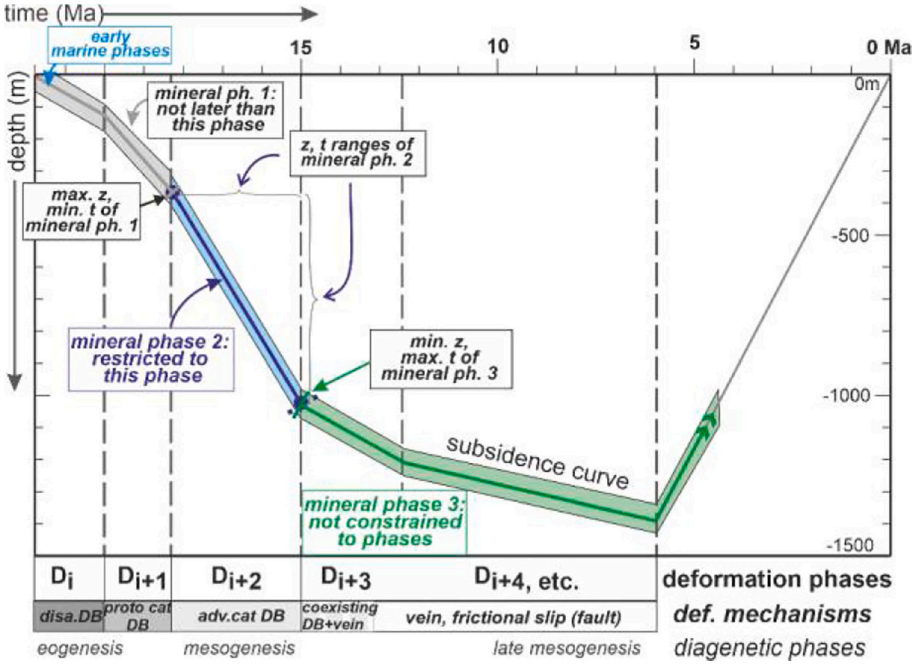

Fig. 2. Simplified concept for integrating constraints derived from distinct type of structural elements, diagenetic alterations and burial history. Min.; minimum, pH; phase, cat:cataclastic, disa; disaggregation bands, adv.; advanced.

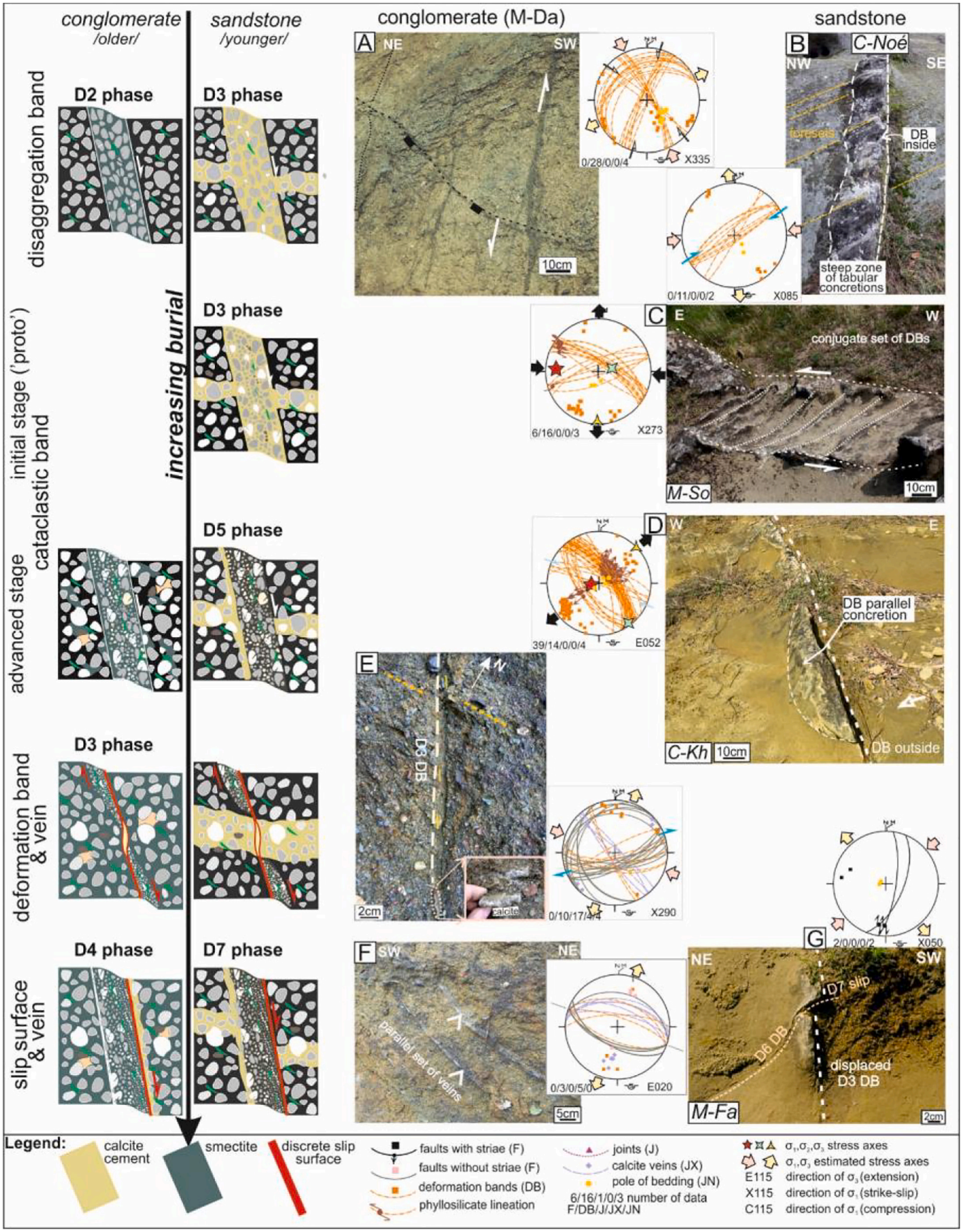

(caption on next page)

Fig. 3. Field photos of different types of deformation elements, stereograms and cementation in chronological order. Note that the timing of change in deformation mechanism is different on the (left) conglomerate and (right) sandstone. A) Two sets of dark coloured, D2 phase disaggregation bands with no relief in host conglomerate at site M-Da. B) Vertical calcite concretion in sandstone along phase D3 disaggregation bands at C-Noé.C) Phase D3, massive calcite cementation along a protocataclastic band with strong relief at M-So. D) Elongated calcite concretion along the outer side (white dashed line)of an advanced stage cataclastic DB (marked by white dotted line) at C-Kh. E) Advanced stage of cataclastic DB having negative relief, alternating with calcite 'pull-apart' domino in conglomerate at M-Da. F) calcite veinlets in conglomerate without DB at M-Da. G) An example of cross-cutting relationship between phase D3 band-related calcite concretion (white dashed lines) and phase D7 (peach dotted lines) deformation element at M-Fa.

in detail). Previously constructed 1D burial models are used for this purpose in the two sub-areas of the present paper.

In this study, we further elaborate this methodology. The basic idea is that (1) distinct types of deformation elements were formed irreversibly with increasing depth (up to the maximum burial); (2) one can connect diagenetic process, including calcite precipitation, their geochemical characteristics (stable isotopes, fluid inclusion data), thus the temperature and origin of fluids from which they precipitated to certain type of deformation elements (DBs or veins). While the burial curve constrains well both the time span and formation depth of structures, these constraints can be transferred to the interconnected diagenetic processes. Using this approach (Fig. 2), the age and burial realm of diagenetic alteration (including calcite precipitation) can be determined. If a calcite phase is characteristic for a given type and age of deformation element, the basin-scale diagenetic processes can be compared (Fig. 2). However, it is important to note that calcite may be formed at a later phase than the host deformation element in some cases.

4. Results

4.1. Field scale observations

Although the observed deformation structures were partly described in Beke et al. (2019), a short presentation is given here in order to demonstrate the connection between evolution of deformation mechanism and diagenetic alterations in the two rock types (Beke et al., 2019). While the Darnó conglomerate is slightly older than the sandstone, the deformation started earlier and the given mechanisms also appeared earlier in this rock type (Fig. 3A,B).

The conglomerates at the Darnó margin of the basin reveal three generation of deformation elements (Fig. 3A, Beke et al., 2019). The oldest generation is represented by three sets of dark bands having no relief. These disaggregation type of bands belong to the earliest, pre-rift phase D2 (Fig. 3A). The next generation of bands (pre-rift phase D3) appears as a single band with negative relief alternating with calcite dominoes along strike (Fig. 3E). Pebbles rotated to parallel to the DB demonstrate that the host rock still had high enough porosity to allow band formation with grain rotation and boundary sliding. However, the opening mode of the calcite dominoes indicates locally consolidated rock. This along-strike variation of structures suggest a mixed mode of deformation between deformation bands and faults (Beke et al., 2019). The following generation of structures is represented by individual calcite veins formed during the early *syn*-rift phase (D4). The deformation mechanism (mode of crack opening) indicates formation in well consolidated rocks (Fig. 3F, Beke et al., 2019).

In the slightly younger sandstone outcrops, the earliest deformation bands belong to the pre-rift phase D3. In a basin centre site (C-Noé), disaggregation bands appear in well-cemented concretions, which are arranged along subvertical zones (Fig. 3B). On the other hand, in the marginal sites (M-Fa and M-So) conjugate pairs of protocataclastic bands with strong relief formed during the same pre-rift phase (D3), (Fig. 3C).

The earliest syn-rift phase (D4) was not represented in the studied sandstone sites but the main rifting events (phases D5 and D6) occur with variably cataclastic DBs. Advanced stage of cataclasis is present in DBs related to the main syn-rift phase D5 at basin centre outcrops (C-Kh, Fig. 3D) and in the cores of borehole C-Sh. The lack of orientation in the latter case does not allow us to connect structures to this deformation phase. At site C-Noé, advanced cataclastic deformation bands alternate with steep calcite veins, geometrically similar to dilational normal faults (Ferrill and Morris, 2003). The calcite veins opened sub-vertically in the pervasively cemented concretions, and directly continue as shear-induced deformation bands in the less cemented host rock. The along-dip variation of deformation mechanisms could occur just before the onset of frictional sliding similarly to structures of phase D3 in the marginal conglomerate (Fig. 3E). In the marginal sites, protocataclastic bands, consistently crosscutting the phase D3 bands were formed related to phase D6 at M-Fa.

The syn-rift bands were reactivated or crosscut by younger fractures during deformation phases D7–D10. At M-Fa, the boundary surface of the phase D6 DB was reactivated as a discrete fault with slightly oblique dextral calcite domino belonging to phase D7 (Fig. 3G). Discrete fracture planes (joints) without calcite cement are present in both central surface sites (C-Noé, C-Kh), and are classified in deformation phases younger than D7 (Beke et al., 2019).

4.2. Host rock petrography

The studied sandstone (PF, Fig. 1) samples are taken from cross-bedded, fine to very coarse-grained sandstone. The sorting ranges from moderate to good and rounding varies within angular to well-rounded. The framework grains are mono- and polycrystalline quartz, feldspar, mica, glauconite sedimentary rock fragments (chert and dolomite), metamorphic and altered igneous rock fragments. The sandstones are classified as litharenite and feldspathic litharenite according to Folk (1974). Along the Darnó Zone (Fig. 1), the studied fan delta conglomerate is represented by poorly sorted, pebbly sandstone and matrix supported polimict conglomerate. The clasts mostly consist of rock fragments, i.e. basic igneous rocks, hyaloclastite, radiolarite and chert (Sztanó and Józsa, 1996).

In sandstone samples of the eastern Darnó margin (Fig. 1), framework grains predominantly show point contacts. In contrast, the samples of the Darnó conglomerate exhibit linear and concavo-convex grain and clast contacts while point contacts are restricted concretions rich in calcite-cement (Fig. 4A). In the sandstones of the basin centre, linear and concavo-convex contacts are widespread (Fig. 4D, F).

In deposits, where the point contacts are observed (Fig. 4C, E), diagenetic glauconite, siderite, pyrite, smectite and calcite are characteristic and mark the pre-compactional diagenetic stage. Glauconite occurs in the intragranular porosity of bioclasts. Siderite crystals form grain-rims around dolomite grains. Siderite and pyrite are present throughout the basin but they are absent in the conglomerate of the Darnó margin. In contrast, grain-rimming (Fig. 4A) and pore-occluding smectite occurs only in the Darnó conglomerate rich in altered basic igneous rock clasts.

Along the eastern Darnó margin, where point contact dominates between the framework grains, circumgranular (Cal1), non-ferroan (pink stained) calcite cement (Fig. 4C), occurs in the sandstone at site M-Fa (Fig. 4C). Elsewhere, the bioclast-rich Darnó conglomerates are cemented by coarse crystalline, non-ferroan, mosaic calcite (Cal2) (Fig. 4A). The calcite-cemented parts of the layers form concretions within the deposits enriched in early diagenetic smectite.

Diagenetic minerals such as albite, ankerite, quartz and calcite engulf linear and concavo-convex grain contacts which indicate they post-dated mechanical compaction (Fig. 4 B,D,F). Diagenetic albite is non-

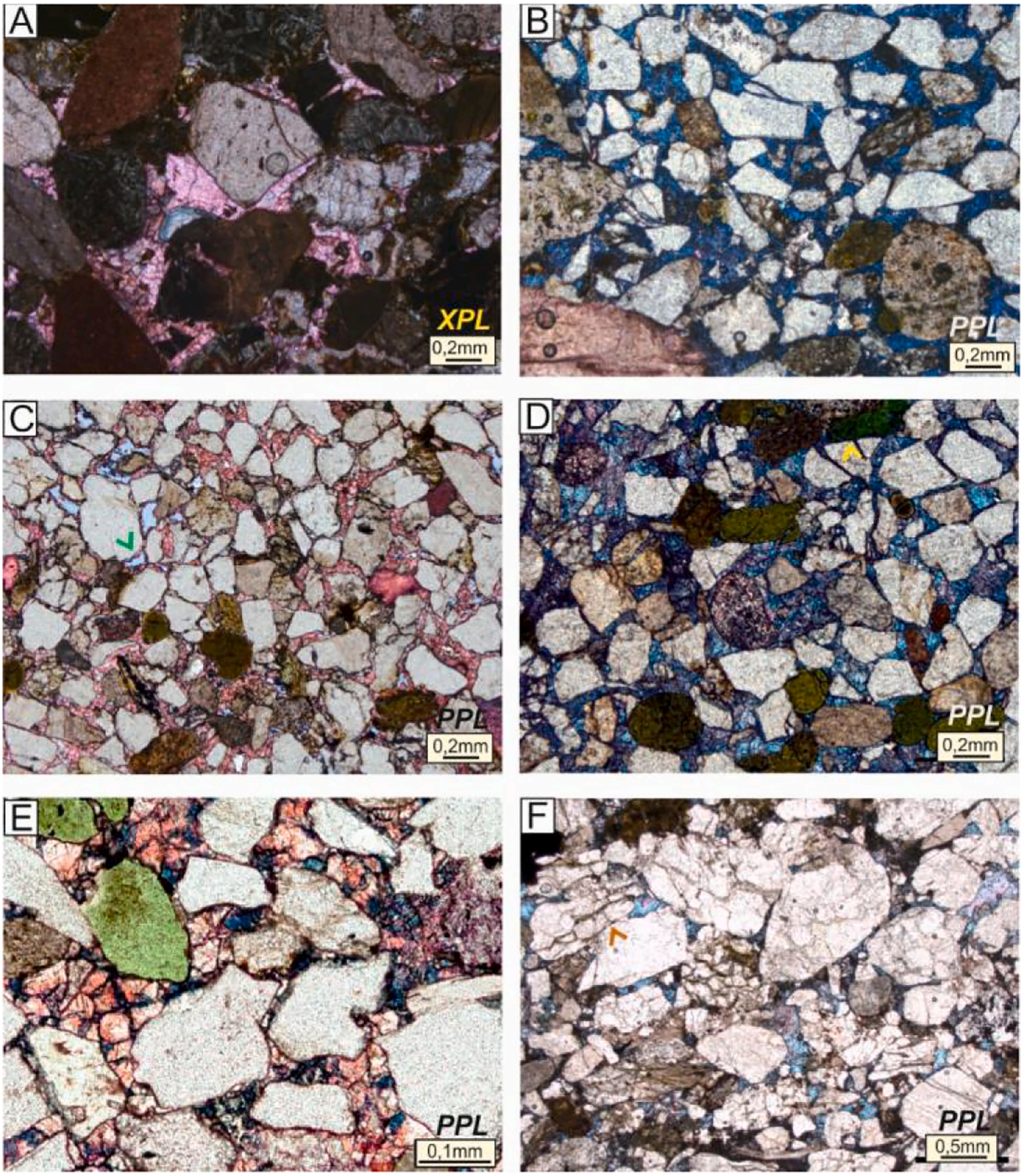

Fig. 4. Photomicrographs of calcite cement generations in host rocks. A) Pink-stained blocky calcite spars (Cal2) in the calcite-rich part of conglomerate of M-Da. A small amount of smectite is present among grains (yellow arrow). B) Blue-stained mosaic calcite (Cal3) occurs in the host sandstone at (M-So), where linear contacts are widespread between grains. C) Pink stained circumgranular calcite cement (Cal1, green arrow) is predominant in the host sandstone at M-Fa. D) Blue-stained calcite (Cal3) in vertically aligned concretions in the sandstone at C-Noé, where grains predominantly have linear contacts (yellow arrow). E) Pink-stained coarse crystalline blocky calcite cement (Cal5) in which point contact dominates between the framework grains and occurs together with a minor amount of blue stained sparry calcite at C-Sh. F) Blue-stained coarse crystalline blocky calcite cement occludes the pores between grains with frequent concavo-convex and linear contacts in the sandstone at C-Kh. (For interpretation of the references to colour in this figure legend, the reader is referred to the web version of this article.)

luminescent and occurs as replacive mottles within detrital K-feldspar and as overgrowth cement on plagioclase grains. Albite is widespread throughout the basin deposits; however, it is missing from the succession of the easternmost marginal localities. Ankerite was observed only in the core section in the central part of the basin (site C-Sh, Fig. 1), as replacing the siderite cement crystals. Minor amounts of microcrystalline quartz and syntaxial quartz overgrowths were detected in the host sandstones throughout the basin. Ferroan calcite (Cal3), characterised by medium to coarse crystal size and blue to mauve staining, occluded the pore space reduced by compaction (Fig. 4 B,D,F). This calcite (Cal3) phase was chiefly observed at the central part of the basin and it is missing in two sites (M-Da, M-Fa) at the eastern Darnó margin.

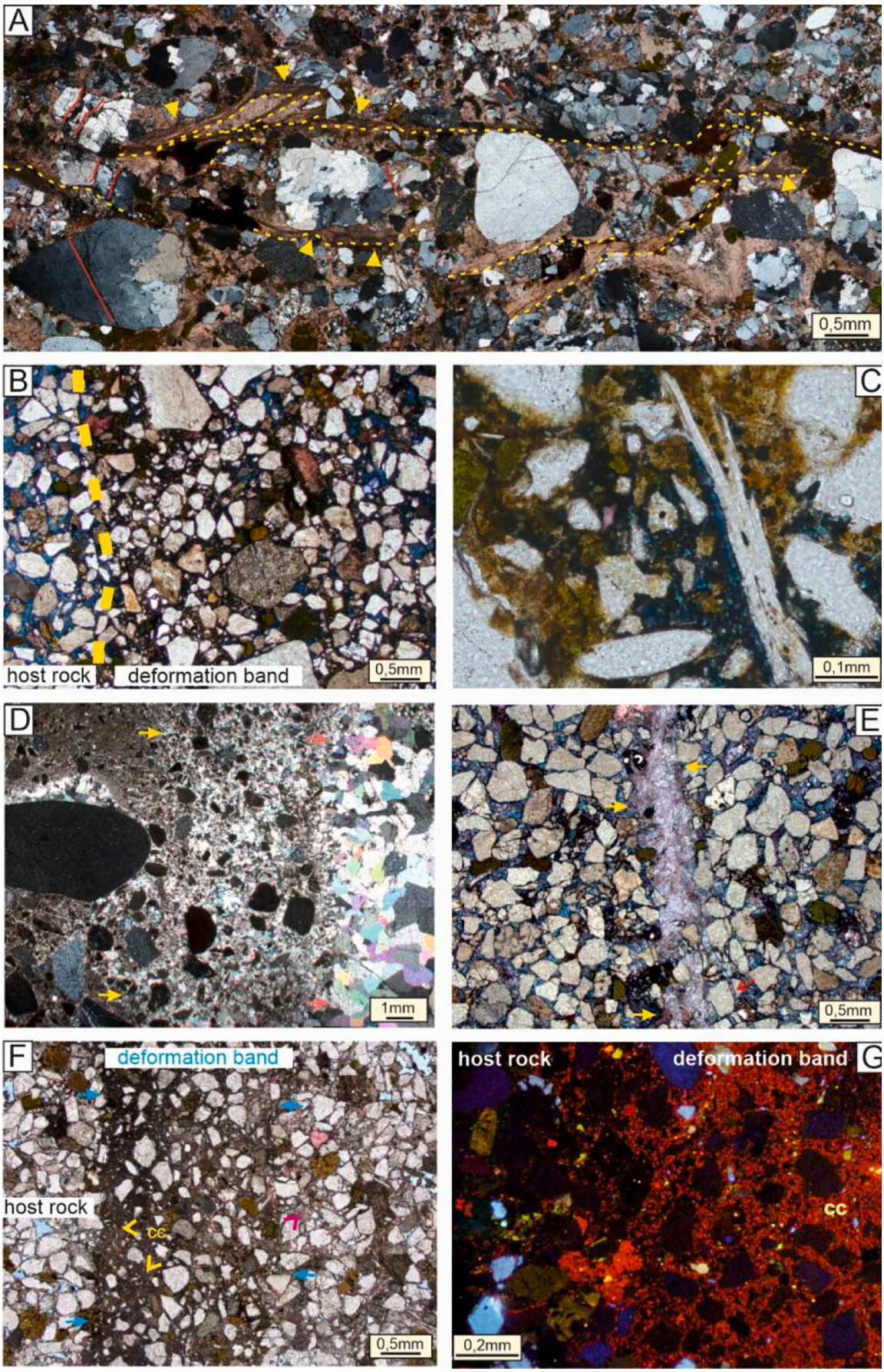

(caption on next page)

Fig. 5. Photomicrographs of calcite cement generations in deformation elements. A) Blocky and fibrous calcite (yellow arrow) occur in disaggregation band (phase D3) from vertical concretion at C-Noé. Calcite fibres in coarser grained and pebbly sandstone indicate shear. B) Blue-stained calcite (Cal4) cement in and along protocataclastic band (phase D3). Calcite cementation is not restricted to the band. Note: this band type requires porous rocks, therefore deformation must have preceded pore occluding cementation. C) Closer view of the previous photo taken in a phase D3 band. The blue stained calcite is microcrystalline and entirely fills the reduced pore space of the DB. D) Calcite domino (phase D3) in conglomerate. The wall is not sharp between the host rock and the domino; instead a 'transition zone' can be followed (between the yellow and pink arrows), where both host rock grains and sparry calcite are present. The pure calcite part of domino (pink arrow) consists of coarse crystalline blocky calcite (red arrows). E) Phase D5 vein (yellow arrow) at C-Noé comprises of mauve-stained blocky calcite crosscutting the concretions cemented by blue-stained (pink arrow) sparry calcite (along phase D3 DBs). F) Reactivated cataclastic DB (phase D6-7) at M-Fa. Reactivation is limited to the left side of the DB and resulted in finer grain size and more matrix (including very fine grained pink stained calcite marked by yellow arrow) than on the right side (calcite in DB marked by pink arrow) of the DB. G) Calcite of the host rock and the reactivated part of the DB shows identical bright orange cathodoluminescence. (For interpretation of the references to colour in this figure legend, the reader is referred to the web version of this article.)

4.3. Petrography of deformation elements

Calcite cements (Cal2,3) within disaggregation bands (Fig. 5A) is medium to coarse crystalline and show similar staining to the adjacent host rock cement. The main difference between the DB calcites of the M-Da and C-Noé sites (Fig. 1) is in the amount of calcite compared to the host rock. In the latter case, where bands are inside calcite concretions (Fig. 3B), the pores between coarser grains are locally enlarged and fully occluded by mosaic, blue to mauve- stained ferroan sparry calcite (Fig. 5E). On the other hand, early diagenetic smectite occludes the intergranular pores in bands formed in the ophiolite-derived (marginal) conglomerate. A minor amount of mosaic, non-ferroan calcite occurs together with smectite, but in a smaller proportion compared to host rocks.

Protocataclastic bands are characterised by minor amounts of frictional matrix derived from minerals which are fragile, ductile (e.g. phyllosilicates) or have good cleavage (e.g. feldspar) (Fig. 5B, C). Although, the porosity and permeability is reduced in bands compared to the host sandstone, the remaining pores are entirely occluded by calcite cement (Cal2 and Cal4) along bands and in the adjacent parts of the host rock. The size of calcite cement decreases from spar to microcrystalline from the host rock through the outer zone of bands toward their core. The calcite (Cal2 and Cal4) microspars are ferroan in the bands of phase D3 (Fig. 5B, C), whereas they are non-ferroan (Cal3) in a later generation of bands of phase D6 (Fig. 5F).

The advanced stage of cataclastic bands are characterised by large

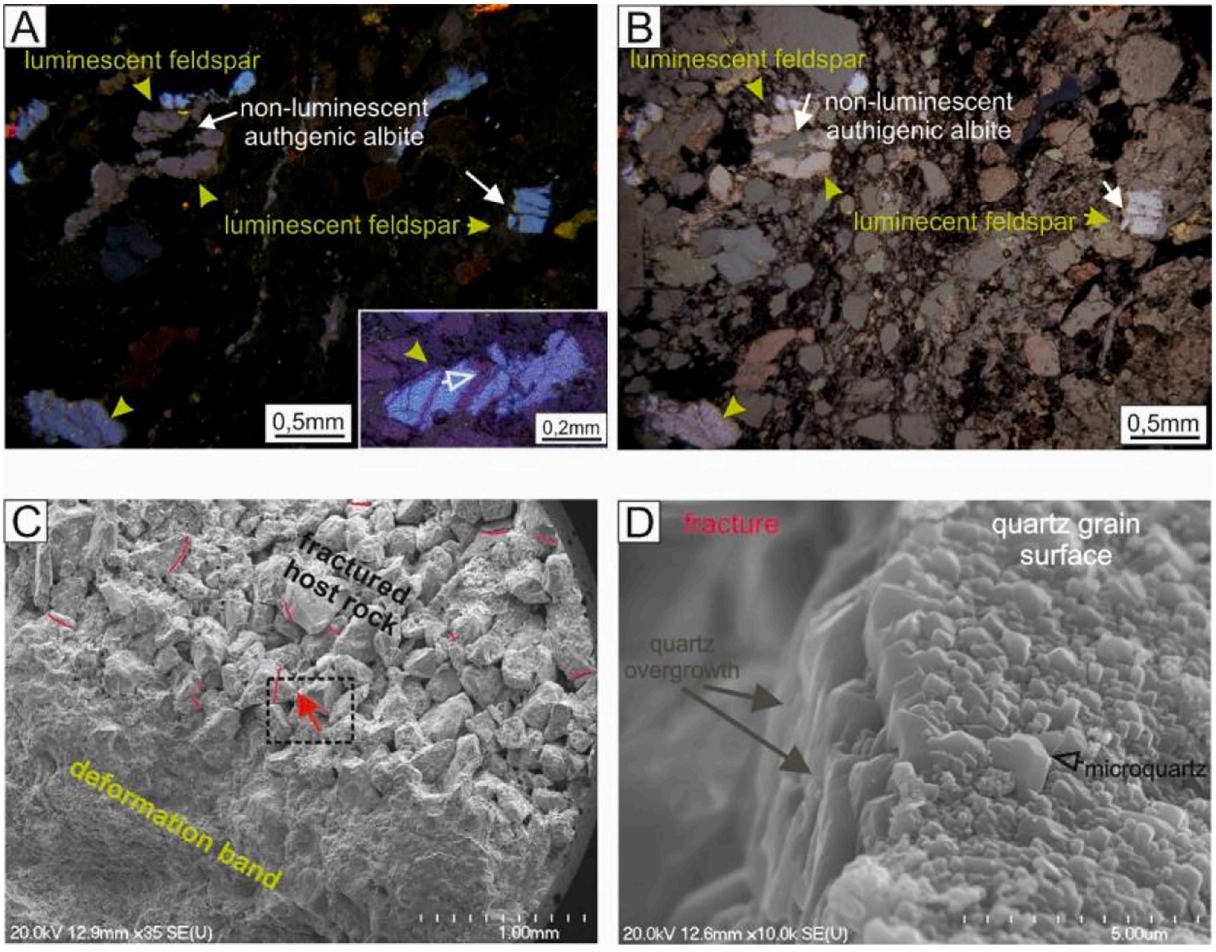

Fig. 6. Photomicrographs: CL and SEM images of authigenic minerals related to the advanced stage of cataclastic deformation bands. A and B) Cathodoluminescent and combined light microscopic(PPL) and CL photo of the core zone of a cataclastic band at C-Kh. Fractured feldspar grains (luminescent) contain authigenic albite (non-luminescent) as a fracture healing pattern. Inset picture shows a closer view of fracture pattern like non-luminescent albite stripes in a feldspar grain C) SEM-SE image of the boundary zone between an advanced stage cataclastic band and the host sandstone. D) SEM-SE photo (taken from the area marked by a dashed rectangle in the photo C) reveals that microcrystalline quartz covers quartz grains, but syntaxial quartz overgrowth occurs on the fracture plane of the grain.

amounts of frictional matrix in which only a few rigid grains remained intact. (Fig. 6B).

In the basin centre, no fractured calcite cement was detected in the bands; however, the host sandstones are cemented by calcite (Cal3). Instead, another type of diagenetic mineral is observed in DBs of the C-Kh. Non-luminescent replacive and fracture-cementing, authigenic albite can be found within feldspar grains both in the host rock and the deformation bands. Adjacent to the band, authigenic albite appears oriented into the direction of shear indicated by the DB (Fig. 6A, B). Syntaxial quartz overgrowths, engulfing microcrystalline quartz on fracture surfaces, occurs preferentially along DB boundary zones (Fig. 6C,D), but cannot be found in the core of the DBs.

At the Darnó margin (site M-Fa), the matrix of the reactivated cataclastic band (phase D7) consists of a small amount of comminuted sedimentary grains among a large amount of fine crystalline calcite (Fig. 5F,G). Both calcite cement phases in the host sandstones (Cal1) and

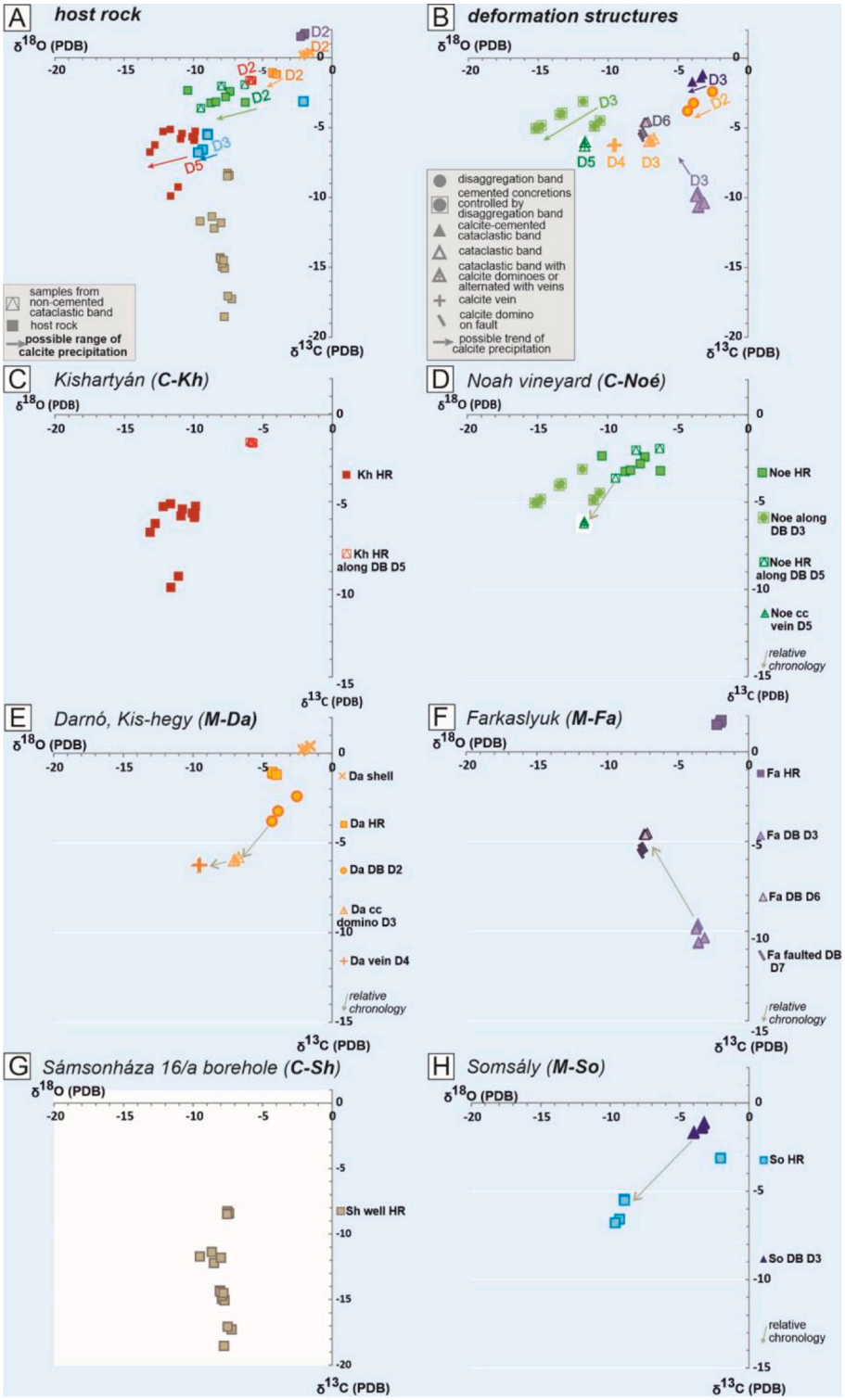

Fig. 7. Cross plots of $\delta^{18}O_{PDB}$ and $\delta^{13}C_{PDB}$ stable isotopic data on calcite cement generations. A) Isotopes of calcite generations in host rock. B) Calcite isotopic values associated with deformation elements. C-G) Stable isotope data trend of the studied sites (the relative chronology of structures marked by grey arrow).

the earlier DB (Cal3) as well as microcrystalline calcite in the bands are non-ferroan and show bright orange CL colour(Fig. 5G).

Calcite dominoes alternate along-dip or along strike with advanced stage of cataclastic bands (Fig. 3E). The opening mode fracture with calcite-fill, occurring together with DBs, is considered a tiny pull-apart structure. In the pervasively cemented part of the host rock, calcite occurs as individual veins without DB (Fig. 3F), which are less than 1 cm in thickness. The veins generally consist of medium to coarse crystalline non-ferroan mosaic calcite (Fig. 5D) at the Darnó margin, whereas calcites are ferroan in basin sites (Fig. 5E). In the case of calcite dominoes, a 'transitional zone' can be observed in the vicinity of the opening between the pure vein and the host rock. In this transitional zone, medium crystalline calcite crystals occluded the enlarged intergranular pore space of the host rock (Fig. 5D). The cement crystals engulf mostly intact grains. In other cases (Fig. 5E), where the vein wall is a sharp zone, only a few isolated fractured grains of the host rock are present among coarse crystalline mosaic calcite.

4.4. Stable isotope data

Bulk rock stable carbon and oxygen isotope compositions of the calcite cement exhibit a clear correlation between the host rock and deformation elements (Fig. 7A,B). The measured calcite phases yielded $\delta^{13}C_{PDB}$ values in a wide range from −18.5‰ to +1.6‰ whereas $\delta^{18}O_{PDB}$ values range from −15.2‰ to −1.3‰. Calcite bivalve and calcite cement in the host sandstones containing circumgranular calcite (Cal1) are characterised by $\delta^{13}C_{PDB}$ values between +1.8‰ and + 0.2‰ and relatively high δ^{18}OPDB values (−1.5‰ to −2.2‰). The majority of isotope data from calcite (Cal2 and Cal3) show a linear trend; $\delta^{13}C_{PDB}$ values vary from −9.9‰ to −1.0‰ and δ^{18}OPDB values yielded a wide range from −15.2‰ to −2.1‰. Host rock bulk samples and most of the cement phases from deformation elements belong to this group. As part of this group, the isotope compositions of calcite dominoes and veins exhibit a particularly narrow range in $\delta^{13}C_{PDB}$ values (between −6.3‰ and − 5.9‰), which is paired with low δ^{18}OPDB values (between −11.7‰ and − 6.7‰).

Two generations of calcite are shifted off the linear trend toward lighter $\delta^{13}C_{PDB}$ values. One calcite generation (Cal4) of phase D3 DBs (at site M-Fa) has $\delta^{13}C_{PDB}$ values of −10.7‰ and − 9.6‰ and δ^{18}OPDB values between −3.7‰ and − 3.1‰ (Fig. 7 site by site). Another calcite (Cal5) phase measured in the host rocks from the borehole sample shows the most negative $\delta^{13}C_{PDB}$ values from −18.5‰ to −8.3‰), whereas the δ^{18}OPDB ratio yielded a narrow range (−9.5‰ to −7.2‰).

4.5. Fluid inclusion data

The observed fluid inclusions in calcite veins at site M-Da are aligned along growth zones and contain a liquid phase. The one-phase liquid filling of these primary fluid inclusions refers to entrapment below cc 50 °C (Goldstein and Reynolds, 1994). The petrographic features and microthermometry data of the studied fluid inclusion assemblages are summarized in Table1. Fluid inclusion (FI) assemblages suitable for microthermometry were only found in the C-Noé samples. The vast majority of fluid inclusions in this sample are aligned along planes. Some of these planes run parallel to each other and represent growth zones, which are mostly outlined by tiny solid inclusions. Fluid inclusions occur sporadically along these growth zones. The largest dimension of these primary fluid inclusions does not exceed 3 μm. They are one or two-phase inclusions containing liquid or liquid+vapour phases at room temperature. All-liquid inclusions are dominant over the two-phase ones within the assemblage. Hence, we suppose that two-phase inclusions formed accidentally, and do not reveal the original fluid density. The small size of these fluid inclusions inhibits their further analysis, including microthermometry. In addition, fluid inclusions occur along planes, running either within the clear crystal cores or crosscutting growth zones. A characteristic feature of the latter textural type is that fluid inclusion planes crosscut only certain growth zones and do not reach the outer rim of the crystals, i.e. they should be regarded as of pseudosecondary origin. These inclusions have an elongated shape and contain one liquid phase at room temperature. The size of these FIs ranges up to 400 μm. In order to determine the salinity of the trapped fluid, we stretched the vacuole of the FIs in order to nucleate a vapour phase. After a stepwise heating process, bubbles finally appeared in them at 230 °C. During subsequent cooling the liquid phase froze at ca. –38 °C in all FIs. During the heating runs, ice melting took place in the presence of a vapour phase, while the last ice crystal uniformly melted at −0.1–0 °C ($n = 13$).

5. Discussion

5.1. Thermal constraints on deformation and the possible origin of associated fluids

Isotopic compositions of calcite generations combined with the calculated formational depth and temperature range of associated deformation elements are applied to determine the possible origin of pore fluid. Hence, this combination of methods involves independent estimations of the potential thermal conditions of basin evolution and related calcite cementation.

The possible depth of deformation was calculated by the integration of relative timing, deformation mechanism and burial curves presented in our earlier works (Beke et al., 2019). The obtained depth constraints are transformed into temperature range using Petromod 1D modelled isotherms based on the Sh-16 borehole considering the average heat flow values (Horváth et al., 2015) in the Pannonian basin during pre-rift and *syn*-rift phases. Additionally, certain authigenic minerals also provided temperature constraints. The initiation of pressure solution-related quartz cement precipitation, which can be related to the temperature limits the maximum temperature of studied sandstone formation. This type of quartz precipitation can also occur at 50 °C, McBride (1989), but become widespread at cc 70–80 °C, Bjørlykke and Egeberg (1993).

The δ^{18}OPDB isotopic data, taking the $\delta^{13}C_{PDB}$ values also into account, are applied as one of the independent constraints on calcite precipitation (based on Kim and O'Neil, 1997). The intersection areas of the temperature range, derived from burial modelling (Fig. 9) and the curve of measured oxygen isotopic values determine the possible range of initial isotopic composition, and hence the possible origin of the fluid (see on Fig. 8).

All the obtained intersections reveal that δ^{18}OSMOW isotopes of pore fluids from which calcites were precipitated fall between −1 and −10‰ (Fig. 8). The δ^{18}OSMOW value of −1‰ is a slightly more depleted than the general Early Miocene (Eggenburgian) marine isotope data (0‰ and + 1‰) published from the Paratethys (Abreu and Haddad, 1998). Nevertheless, the one of the extreme value (−10‰) of the recalculated $\delta^{18}O_{SMOW}$ of the fluids is close to the modern meteoric water for this latitude (ca.–10‰, Virág, 2018) at 0–200 m topographic elevation. Similar Miocene isotopic values were reported in sandstones from fresh groundwater affected systems in other regions at similar latitude (e.g. Milliken et al., 2009; Balsamo et al., 2012). These isotopic constraints on end-member fluid compositions together with positive correlation between wide range of $\delta^{18}O_{PDB}$ (−15.2‰ to +1.3‰) and $\delta^{13}C_{PDB}$ values can be either interpreted as variable amounts of calcite phases or mixing between the fluid end-members in variable proportions (Banner and Hanson, 1990).

Considering the lack of evidence for marine cement in the majority of the samples (Szőcs and Hips, 2018) and single-phase vein opening (supported by vein texture, no signs of crack and seal), we assume variable proportions of mixing between meteoric and connate marine pore waters. However minor amounts of co-occurring calcite phases are present in some samples (C-Sh borehole).

In addition, both all-liquid aqueous inclusions and the presence of

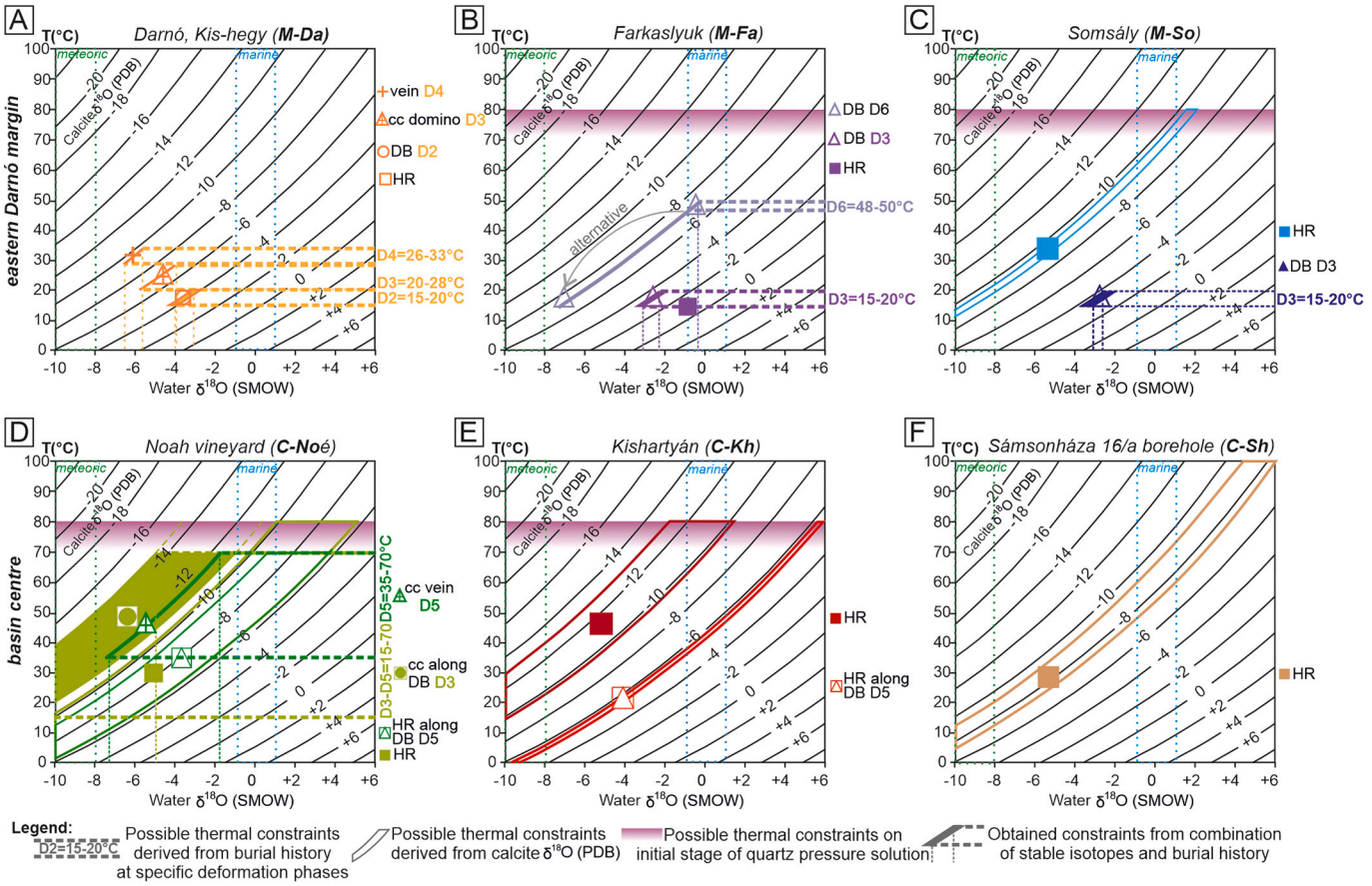

Fig. 8. Estimations of possible pore fluid compositions based on temporally well-defined calcite generations. Constraints are gained from the combination of δ^{18}OPDB isotopic data of calcite using Kim and O'Neil's (1997) equation and the possible temperature ranges derived from 1D burial modelling (Fig. 9). The intersected area projected to x axis determines the potential $\delta 18O_{SMOW}$ values. The oxygen isotopes of the original pore fluid are characteristic for waters between marine and meteoric types in all cases (A-F).

Table 1
The petrographic features and microthermometry data of the studied fluid inclusion assemblages.

Sample ID	FI genetic type	Phase assemblage @Troom	Trapping temperature	Tm(Ice)	Size
M-Da	P	L	<50 °C	n.d.	<5 μm
C-Noé	P	L (L + V, rare)	?	n.d.	<3 μm
C-Noé	PS	L	<50 °C	−0.1-0 °C (13)	<400 μm

the extremely low-salinity fluid trapped in the pseudosecondary inclusions of calcite veins (C-Noé, Table 1), further supports the contribution of meteoric fluid source.

As the variable ratio of admixing between two types of fluids is the most plausible explanation for the wide range of $\delta^{18}O_{PDB}$ values paired with a gradual decrease in $\delta^{13}C_{PDB}$ values, calculations were carried out on the possible temperature range of precipitation for both end-member cases ($\delta^{18}O_{SMOW}$ −10‰ and −1‰). A paragenetic sequence tied to burial curves provides additional constraints to the obtained values (Fig. 9). The gradual change in isotopic composition (Fig. 7) together with the different types of deformation mechanisms serve as input constraints for reconstructing the timing of cementation (Fig. 9). In the following, we discuss the possible temperature range and origin of calcite generations in chronological order inferred from structural evolution and burial modelling. Uncertainties are present in the preliminary assumptions such as estimated burial depth (±100–150 m corresponding to 5–7 °C), geothermal gradients (±2 °C within 100 m) as well as the postulated timing of cementation. In addition, we should take into consideration that meteoric water supply circulating downward can be (several degrees) cooler than the expected host rock temperature.

At the eastern (Darnó) margin, the earliest band generation (phase D2) and one host rock sample (M-Da) exhibit slightly more negative δ^{18}OPDB and $\delta^{13}C_{PDB}$ isotope values (Fig. 7E) than supposed marine values. This band generation is relatively enriched in smectite and the remaining pore space was occluded by calcite with similar composition to the host rock. Preferential smectite enrichment was reported and interpreted by Wilson et al. (2006) as an early diagenetic record of meteoric fluid flow through DBs in non-welded ignimbrites. Both the presence of early diagenetic smectite and the isotopes of coeval or subsequent precipitation of non-ferroan calcite suggest slightly modified marine water (Fig. 8).

The subsequent D3 phase of cataclastic DBs alternated with calcite dominoes (M-Da) has significantly less depleted isotopic ratios than phase D2 band (Fig. 7E), which corresponds well to their younger structural chronology. This argument refer to pre-rift, early phase D2 band cementation (presumably together with host rock calcite) prior to phase D3. Calcite dominoes related to phase D3 could have precipitated at temperatures between 20 °C and 28 °C. The early phase D3 bands in sandstone of the two other marginal sites (M-Fa, M-So) have similar δ^{18}OPDB isotope values compared to the phase D2 band in conglomerate. The significantly lower $\delta^{13}C_{PDB}$ values adjacent to one of the D3 bands (Fig. 7F) suggest that pore water may have been locally contaminated with fluid rich in organic material during or shortly after actively forming D3 bands. The additional amount of light carbon can

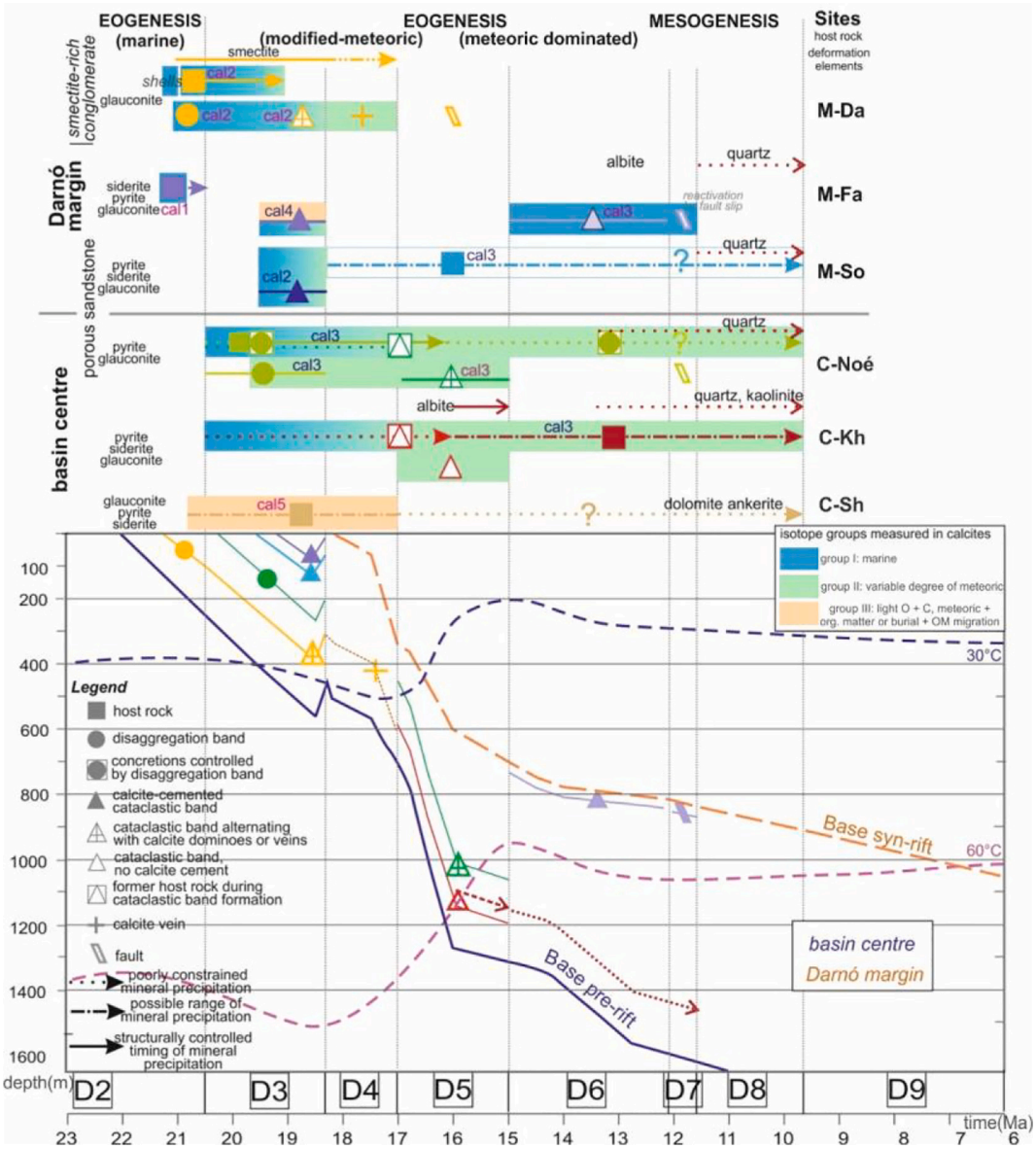

Fig. 9. Paragenetic sequences of the studied sites combined with simplified burial curves (using Petromod 1D, after Beke et al., 2019). The paragenetic order is placed in the context of the main recognised diagenetic components and deformation structures. Time constraints on cement generations are based on the relationship of calcite and structural elements during subsidence. The transition between eogenesis and mesogenesis are determined by burial depth related temperature (~70 °C) instead of the connectivity of pore water with meteoric waters (Morad et al., 2000).

derive from oxidation of organic matter either by upward migration from deeply buried organic-rich source rock or by meteoric fluids passing through organic-rich sediment. Indeed coal-bearing formation deposited almost directly on the studied pre-rift sandstone during the D4 deformation phase (18.2–17 Ma). In this scenario cementation would fall into this time span, after D3 band formation while the deposition of the coal-bearing strata post-dates the formation of D3 bands. On the other hand, the presence of deeply-seated organic-rich sediments, the possibility of oil generation and migration at the time of deformation together with well-known hydrocarbon occurrences both at the Darnó margin and in the basin centre support upward migration (Kovács et al., 2020). In this case, the outstanding carbon isotope values can be considered as a local factor in fluid composition at the time of precipitation.

All together phase D3 structures in the eastern (Darnó) margin with calcite cement having more depleted $\delta^{18}O$ value (−7.1‰ and − 2.5‰) could have formed between 0 °C and 46 °C assuming meteoric and marine end-members, respectively (Fig. 8A,B,C). Burial history (Fig. 9) indicates that these temperature values are roughly between 15 °C and 28 °C. This burial constraint together with the carbon isotopic ratio (−10.7‰ and −1.2‰) suggest modified marine pore fluid, excluding pure meteoric water (Fig. 8A,B,C).

At the basin centre, the vertically aligned concretions along phase D3 disaggregation bands (Fig. 3B) might have precipitated at 18 °C to 101 °C. Considering the thermal evolution of the basin together with the initial stage of quartz pressure solution in the sandstone samples, temperature above 80–90 °C is not realistic in this part of the Pannonian Basin. Therefore, the the initial pore fluid composition was limited between modified marine and meteoric water. The wide range of $\delta^{18}O_{PDB}$ (Fig. 8D) isotope values together with gradually varying carbon isotopes in the phase D3 band associated concretions may have resulted from the fact that the temperature of the pore fluid increased together with the proportion of meteoric involvement in line with time. However, phase D3 deformation is the earliest possible formation period, the main period of vertical concretion formations could have lasted between phases D3 and D5 based on the systematic crosscutting relationship with

phase D5 veins (Fig. 5E). The wide range of isotopic composition may reflect temporally continuous growth during ongoing subsidence.

The phase D4 individual calcite vein as the earliest *syn*-rift structure occurred only at eastern (Darnó) margin exhibits even more depleted δ^{18}OPDB isotopic values than the previous calcite phases (Fig. 7E). The observed shift in oxygen isotopic values may refer to an increase in temperature. The onset of rifting could have increased the heat flow, thus the temperature even at shallow burial depth. The increased temperature could have induced diagenetic alterations (van Balen and Cloetingh, 1993). Phase D4 veins may reflect temperatures between 13 °C and 61 °C, while burial depth calculation suggests a narrower 26–33 °C interval during this phase of deformation (Fig. 8A). The primary single-phase fluid inclusions in this calcite vein generation also indicate entrapment below cc 50 °C (Goldstein and Reynolds, 1994). The obtained temperature suggests precipitation from significant freshwater contribution admixed to residual marine pore water (Fig. 8A). Many similar calcite veins of meteoric origin have been reported from sandstones (e.g., Eichhubl et al., 2009; Milliken et al., 2009; Andre et al., 2010; Beaudoin et al., 2014; Bertotti et al., 2017; de Graaf et al., 2017). The isotopic range of some of the described calcite veins and their potential formation depth are comparable with our examples.

The phase D5 structures occurred only at the basin centre. The δ^{18}OPDB (around −11‰) of phase D5 veins permits temperatures of 23 °C to 75 °C, but the isotherm calculated from modelling proposes narrower interval (35 °C to 70 °C) for host rock temperature during vein precipitation (Fig. 8D, Fig. 9). According to all-liquid aqueous inclusions, we suggest trapping below 50 °C in the case of this assemblage. The extremely low-salinity pseudosecondary fluid inclusions of C-Noé represent an intermediate meteoric fluid signal during the precipitation of the fracture-filling cement.

In the case of the phase D5 cataclastic deformation band other independent thermal indicators also helped determine the possible temperature of the host sandstone during deformation. The presence of fracture healing authigenic albite (Fig. 6A, B) in phase D5 band refers to minimum 60–65 °C (Saigal et al., 1988). In contrast, the microcrystalline quartz and subsequent quartz overgrowth occur only in the porous, slightly deformed boundaries of the band (Fig. 6C, D), but they are completely missing on the quartz grains in the core of bands. This evidence indicates post-deformational syntaxial quartz overgrowth, which might have took place between phases D6 to D8 during burial (Fig. 9). According to these thermal indicator diagenetic minerals, we envisage that phase D5 deformation took place roughly between at 60 °C and 80 °C. All these above described constraints suggest 23 °C to 50 °C for fluid and 35 °C to 70 °C for host rock temperature during phase D5 deformation.

The subsequent phase D6 of DBs at the eastern (Darnó) margin (site M-Fa) show δ^{18}OPDB values similar to those measured in phase D3 calcite dominoes at site M-Da (Fig. 7). Based on burial history, D6 bands could have formed at a burial depth where 48–50 °C temperature was assumed (Fig. 8B). This burial constraint suggests that the calcite of D6 bands might have precipitated from heated marine pore waters that were enriched only in light carbon (−6‰). Nevertheless an alternative explanation to the shallower burial meteoric origin of bands related to phase D6 cannot be ruled out on the basis of isotope values and the deformation mechanism (similar to phase D3 bands) that is characteristic of shallower depths (Fig. 8B).

The next temporal tie point is the reactivation of the previous, phase D6 band as a very narrow fault zone (D7), where the earlier generation of calcite cement was comminuted during frictional slip. This faulting also displaces stratabound concretions. The reactivated structure serves as an upper time constraint for cement precipitation in previous phase D6 deformation bands.

Overall, the central and marginal sites, the relative chronology of the studied deformation structures in agreement with the deformation mechanism suggest that the preserved records of fluid-flow mainly formed during the phases D2 to D6 (Fig. 9). The progressive temporal depletion trend in isotopic ratios can be attributed to the increasing ratio of the meteoric component (Fig. 8A) in pore fluids accompanied with a parallel increase in temperature and burial depth. The evolution history started with early and modified marine records during pre-rift deformation phases (D2-D3) and meteoric component became more dominant in the cement generations of the main *syn*-rift phases (D4–D6) of the intense subsidence. The lack of calcite cement associated with structural elements younger than the D6 phase suggests that favourable conditions for structurally controlled massive calcite cementation ceased before phase D7 deformation.

Host rock calcite cement is poorly constrained temporally and possibly includes several calcite generations compared to deformation structures. In some cases, the uplift-related telogenetic origin of host rock calcite cannot be excluded.

Based on a systematic depletion trend in isotope ratios from the older to the younger phase of calcite generations (Fig. 7), one would expect identical values for each phase of calcite generations formed at similar burial depth. On the contrary, in site M-Da, older structures show similar isotope ratios to younger ones at the other sites (M-Fa, M-So). This apparent contradiction can either be resolved by different burial position at the time of calcite precipitation, or local spatial variation in the rate of meteoric water infiltration. In the following, we infer the proposed time of host rock cementation by combination of comparable isotopic values and relationship with deformation structures (Fig. 9).

Concretion formation was widespread in eastern marginal sites all along structural elements, while the pervasive host rock cementation occurs only at sites M-Da and M-So. Calcite of host conglomerate (M-Da) which is present together with smectite can mainly be attributed to phase D2 based on the trend in isotopic values. Pervasive calcite cementation in the host sandstone (at site M-So) can only be later than the encasing phase D3 bands (Fig. 3C). Therefore, isotopic signals of the host sandstone can represent a later stage of cementation than the D3 phase band's (Fig. 9). These values are comparable to D4 veins in the conglomerate at M-Da (Fig. 7).

At the other marginal sandstone site (M-Fa) the host rock is poorly cemented with early marine calcite (Cal-1) and only a few stratabound, partly asymmetric concretions occur at one side of the pre-existing bands. The presence of both displaced and non-faulted, but asymmetric stratabound concretions may refer to continuous layer parallel concretion growth before and partly after the last phase (D6) of DB formation.

The two outcrops of the basin centre (C-Noé and C-Kh) show an overlapping range of isotopic signals (Fig. 7C, D), which may allow narrowing the timing and origin of host rock cementation (Fig. 8D). The calcite of C-Noé's host rock (Fig. 7D) might have existed at the time of phase D5 band formation (Fig. 7C,D), because these bands behave as barriers to later fluid flow. On the other hand, we assume that the veins at C-Noé as well as stratabound calcite concretions at C-Kh could also have precipitated from meteoric water or fluid with significant meteoric component based on the similarity in their isotopic ranges (Fig. 7C, D). The stratabound cementation of the host rock at C-Kh could have formed shortly after the phase D5 deformation and partly coeval with the quartz overgrowth (Fig. 6C,D) together with kaolinite (Fig. 9). However, the telogenetic origin of calcite cannot be excluded at site C-Kh (Szőcs and Hips, 2018), the similarity of isotopic values to the phase D5 vein at C-Noé (Fig. 7C,D) rather supports formation closely after phase D5 deformation.

The borehole C-Sh deviates from the general trend due to the wide range of more negative $\delta^{13}C_{PDB}$ isotopes and a narrow spectrum of δ^{18}OPDB isotope values (Fig. 7G). The relative homogeneity of δ^{18}OPDB and the high variability of $\delta^{13}C_{PDB}$ can be a characteristic of a meteoric phreatic system water line (Lohmann, 1988), but the very low $\delta^{13}C_{PDB}$ isotopic values together with the presence of bitumen traces in pores may refer to the involvement of hydrocarbon-bearing fluids. Microscopic evidence implies that the predominant calcite cement (Fig. 4E) is pre-compactional which refers to a relatively shallow burial origin

(Szőcs and Hips, 2018). The comparison with other calcite generations in more compacted host rocks (Fig. 4B,D,F) indicates that calcite precipitation was earlier than the intense subsidence of phase D5. This assumption constrains the timing of the cementation during the pre-rift (D2 and D3) or early *syn*-rift (D4) phases (Fig. 9).

5.2. Model for the evolution of the fluid flow system during the deformation history

The structural diagenetic evolution is distinctly expressed in the eastern marginal and central areas during progressive burial. This spatio-temporal difference is expected because the Early Miocene pre-rift basin was subject to folding and thrusting, and the deformation mostly concentrated on the eastern (Darnó) margin with contractional character (Fig. 1C,D,E).

The basin margin outcrops recorded the earliest diagenetic alterations, which started with marine calcite and (Fig. 7) followed by the increasing influence of meteoric water during successive D2 and D3 deformation phases. These structural records are attributed to the pre-rift history in a ~ 4 Ma long time span, from 22 to ~18 Ma. Similar shallow burial, meteoric calcite cementation is frequently attributed to compressional deformation (e.g. Travé et al., 1998; Mangenot et al., 2018). The infiltration of meteoric water could possibly be initiated along the basin margin due to active deformation and the elevated hanging wall of thrust faults.

The pre-rift evolution occurred at very shallow burial depth from 0 to 400 m, in agreement with the type of deformation structures (Fig. 9). In site M-Da, located at the base of the clastic formation, calcite precipitation started from 0 to 100 m (phase D2) related to disaggregation band that requires still unconsolidated sediments. However, in the slightly younger part of sandstones at sites M-So and M-Fa, the calcite of phase D3 deformation band could have also formed between 0 and 150 m depths (Fig. 9). This narrow and comparable depth range for the formation of phase D2 and D3 DBs and associated calcite phases correspond well to the overlapping isotopic composition of pore fluids (Fig. 7B). Already during the late stage of D3, but definitely from phase D4, calcite precipitated in the Darnó conglomerate as dominoes and veins between 300 and 600 m depth (Fig. 9).

The change from pre-rift (phase D3) compression-transpression to *syn*-rift (D4) extension tectonics does not correspond to significant change in the isotopic composition of the circulating fluid (Fig. 7B). Oxygen isotopic values were only slightly shifted toward more depleted values referring to elevated temperature in line with greater depth and heat flow. The switch in deformation mechanism from deformation band to vein formation indicates that the host conglomerate uniformly reached the consolidated state at that time (Fig. 3F). On the contrary, the studied sandstone remained relatively porous rocks allowing DB formation and considerable fluid-flow during the entire pre-rift and in the early syn-rift stages. The presence of the early type of cataclastic DBs related to phases D3 and D6 at site M-Fa suggests that host rock petrophysical parameters might have not changed significantly between the two deformation phases. This may be related to a specific syn-rift burial history of this site (Beke et al., 2019).

In contrast, in the basin centre, syn-rift structures are predominant, which are represented by an advanced stage of cataclastic bands and discrete fractures (veins, fault-slip). The switch to discrete frictional slip and vein opening in sandstone may have occurred between 400 m and 1200 m depth (Fig. 9) during or shortly after the accelerated subsidence related to phase D5. Isotopic signals clearly reflect the increased contribution of meteoric water in pore fluids expressed both in calcite generations along earlier (phase D3) DBs and in phase D5 veins. This possibly coincide with the pervasive cementation of the host sandstone which could have also occurred when subsidence was the fastest and fracturing the most intense during the syn-rift phases (Figs. 9, 10). The estimated fluid temperatures related to syn-rift phases refer to hotter water in basin centre sites than along the Darnó margin (compare C-Noé on Fig. 8D and M-Da, Fa on Figs. 8A,B), partly because M-Da veins represent an earlier and shallower stage (D4) of subsidence. The increase in temperature during syn-rift phases (Fig. 7B) can be attributed to the deeper burial depth of the central sites than the marginal ones. However, no calcite cement related to deformation elements was observed younger than phase D5 in the central sites. The wider spectrum toward more depleted isotopic ratios at C-Noé (Fig. 7D) suggest that water percolation might have continued during the subsequent D6–D8 deformation phases (depth can exceed 1400 m, Fig. 9).

We envisage that the studied porous sandstone and conglomerate

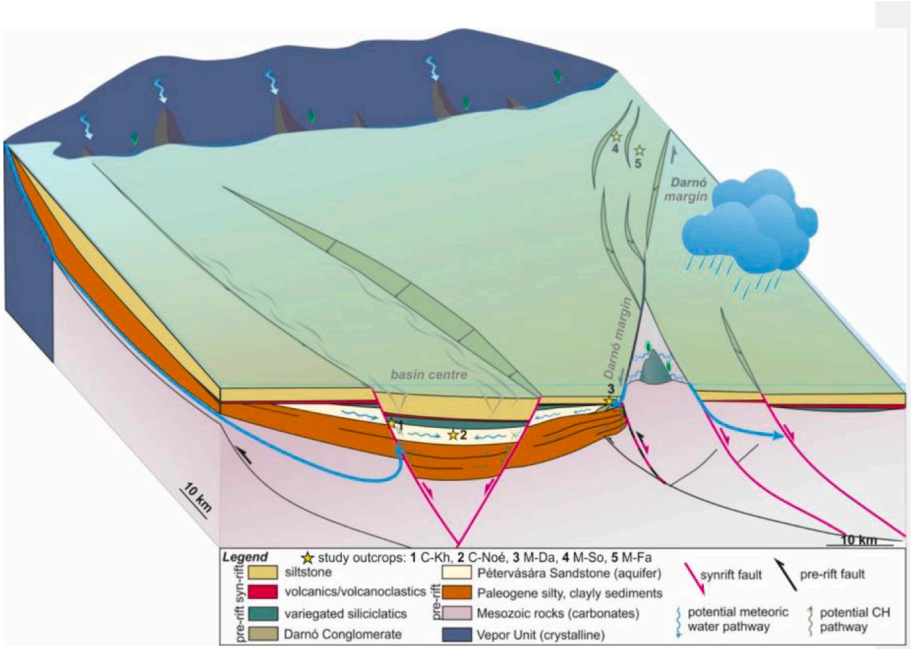

Fig. 10. Schematic model showing potential fluid flow pathways during the main syn-rift phases based on seismic (Kovács et al., 2020) and geological cross-sections (Beke et al., 2019).

may have acted as regional aquifer located between aquitard sediments in a basin-scale fluid flow system (Fig. 10) and permitted considerable fluid flow. Large-scale circulation was possible because pre-rift sandstone dipping toward the basin centre were exposed or were shallowly buried at all margins of the rift systems. In the north, the Vepor crystalline and all pre-rift formations were tilted to the south and exposed during the early part of the rifting, and only covered by ca. 15–13 Ma volcanoclastics. Near the eastern Darnó margin, within the Darnó Zone and in the Bükk Mts. Mesozoic carbonates prone to karstification formed the margin of syn-rift grabens (Figs. 1D, E and 10). At the western margin (Buda Hills), the western occurrences of the pre-rift sandstone were elevated within the footwall of large-displacement syn-rift faults (Fodor et al., 1999). From these potentially elevated areas (Fig. 10) the gravity-driven recharge systems allowed the continuous percolation of meteoric water that diluted residual connate pore fluids. The fluid-flow toward deeper parts of the basin was coupled with the gradual heating of circulating fluids. The water moved in sandstone aquifers primarily along bedding planes and large faults, as demonstrated in basin-margin carbonates by fluid flow modelling (Havril et al., 2016). During water circulation, a specific type of early deformation bands and fractures cut across beds and provided avenues for vertical 'transbedding' fluid flow (Fig. 10). The lack of calcite in structural elements after the main phases of subsidence may suggest that percolating water was either no longer saturated for cement precipitation or it could not enter this aquifer due to sediment cover. The ongoing subsidence reached its maximum around 8 Ma (~1.5 km), ~10 Ma after the rift initiation. This was followed by neotectonic inversion, uplift (Arató et al., 2019) and denudation, but these left little trace in the study sites.

5.3. Relationship of deformation structures and fluid flow

Based on meso-, and microscopic observations together with isotopic data of structurally controlled concretions, shallowly formed (<1 km) deformation elements have variable relationship with fluid-flow.

5.3.1. Disaggregation band

This band type together with the intersection of coarse-grained strata favoured massive calcite precipitation resultedin vertically alignedcemented concretions (Fig. 3A) in the sandstone. Such intersections, where the porous space is the largest, certainly provided a preferential path for fluid flow. Meanwhile, in the Darnó conglomerate, disaggregation bands favour the formation of early diagenetic smectite in agreement with earlier observations on DBs (Wilson et al., 2006).

Stable isotope data of calcite in disaggregation bands partly overlaps and shows the δ^{18}OPDB and $\delta^{13}C_{PDB}$ depletion trend of host rock data. The overlapping isotopic signatures suggests that calcite precipitation in the host rock and in the bands can be regarded as concurrent processes. This interpretation agrees well with the general observation that the disaggregation band has no significant porosity change with respect to the host rock (Fossen et al., 2007). However, the earliest type of deformation bands is likely to preserve the earliest records of fluid-flow suggesting that they rather enhanced diagenetic alterations It is in accordance with our earlier observations that if the host rock is at least partially cemented, this type of band also contains cement (Beke et al., 2019).

5.3.2. Protocataclastic bands

The observed pervasive cementation (Fig. 3C,G and Fig. 5B, C) in this type of bands (M-Fa, M-So) indicates that calcite precipitation favoured these structures. Carbonate cemented protocataclastic type bands were only described in a few places (Balsamo et al., 2012; Skurtveit et al., 2015; Lommatzsch et al., 2015b; Del Sole and Antonellini, 2019). The work of Lommatzsch et al. (2015b) assumed that the massive cementation of DB preserved the early phase of dilation during band formation. We cannot recognise dilation within the studied DBs, and hence we rule out this possible explanation in our case. On the contrary, Del Sole and Antonellini (2019) argue that fluid flow was retarded in the case of band associated tabular calcite concretions (CSB). Their study hypothesis is that carbonate cementation is promoted by the combination of decreased porosity which slowed down fluid flow and the presence of a great amount of reactive feldspar grain surfaces derived from comminution. In our case, massive cementation is not restricted to the bands but expands symmetrically into the surrounding host rock resulting in tabular concretions of several centimetres in thickness along bands of a few millimetres –1 cm thickness. Hence, the combination of retarded fluid flow and reactive grain surfaces cannot solely explain the extensive cementation. Despite the fact that grain size and porosity reduction are in apparent contradiction with the promotion of fluid flow (except when assuming capillary suction), we suggest that porosity contrast along the outer and inner zones of bands plays a role in massive cementation. We speculate that the breaking of grains, in the outer zone of band, creates additional fracture porosity and more reactive fresh grain surfaces without significant grain size reduction and pore occluding matrix. Although porosity in the core zone of bands has reduced, it still remains permeable enough for fluid migration. Thus, the enhanced cementation of bands compared to the host rock can be the result of local decrease in pCO_2 or the consequence of fluid mixing during increased fluid-flux along the outer zone of bands.

Considering isotopic composition, Balsamo et al. (2012) reported isotopic values (δ^{18}OPDB –6‰ and − 1‰ paired with $\delta^{13}C_{PDB}$ between −4‰ and 0‰) from the Crotone basin (Italy) from concretions related to the early type of DBs. Their measured isotope values were interpreted as precipitation in mixing marine and meteoric vadose zone during eogenesis, which can be the case for the D3 and D6 bands of this study. Skurtveit et al. (2015) demonstrated isotopic data from calcite of a similar cataclastic band that differs from the host rock values, but no further explanation was given for the deviating record.

Due to all the reported and demonstrated calcite in protocataclastic bands differs from host rock, and even from different phases of calcite in isotopic ratios (M-Fa site, D3 and D6, Fig. 7F), these early structures are capable of preserving distinct records of fluid-flow evolution, which cannot be identified in the undeformed host rock. These arguments also suggest that the different conductivity properties of structural elements and host rocks cannot be accounted for by the variable degree of mixing in these cases.

5.3.3. Advanced stage of cataclastic bands

Carbonate cement was not identified in this type of deformation bands, which suggests that this type of band behaves as barrier to fluid flow (Fossen et al., 2007; Torabi and Fossen, 2009; Fossen et al., 2017; Shipton et al., 2005; Ballas et al., 2012; Tueckmantel et al., 2012; Torabi et al., 2013). Hence, these bands can provide clues to the former state of host rock alterations at the time of deformation. This behavior of the bands contributed to narrowing the time constraints of calcite and other diagenetic minerals, whether or not was present (at least locally) in the host rock pores. In our special case, deformation band related diagenetic albite (Fig. 6A,B) could have precipitated after initial fracturing, but before the greatest porosity reduction in the core zone of bands, while later diagenetic minerals (calcite, syntaxial quartz overgrowth) are missing.

Isotopic data from these bands show similar values in both sites, and the signatures overlap with those of the host rocks in one of the sites (C-Noé, Fig. 7C, D). In site C-Kh, where isotopes of calcite in the DB and in the host rock are different, pervasive cementation of the host rock postdates DB formation. This evidence also strengthen that isotopic values in bands can represent the calcite phases of the host rock at the time of deformation.

5.3.4. Calcite dominoes and veins

Calcite dominoes and veins (M-Da, C-Noé) formed partly together with the advanced stage of cataclastic bands (Fig. 3E). This combination of two different types of deformation mechanism is considered to be an

important step in diagenetic evolution when part of the host rock layers has been cemented while others still have enough porosity for band formation (Davatzes et al., 2003; Beke et al., 2019).

All the isotopic values (Fig. 7E) of calcite veins and dominoes (Fig. 7B) exhibit very similar $\delta^{13}C_{PDB}$ isotopic signals (around −6‰). The shift between subsequent calcite generations (phase D3, D4 and D5) toward more depleted δ^{18}OPDB isotopic values can be mostly attributed to increasing temperature in line with burial depth.

On the whole, distinct types of deformation elements have variable behavior to fluid flow, which also manifested in variable isotopic records of the associated cementation (Fig. 7B). Comparing stable isotopic signatures of calcite in the host rocks (Fig. 7A) and in the deformation elements, host rock cementation seems to at least partly independent from the deformation structures of good conduits.

6. Conclusions

1) The combined application of temporally variable deformation elements, stable isotopic and fluid inclusion data of cement generations and burial modelling proved to be a powerful tool for the determination of the source of fluids and can be useful in sedimentary basins worldwide.
2) Structural elements of variable age preserved distinct temporal records of fluid composition and temperature. The projection of deformation band related calcite isotope data to the subsidence curve provided constraints for the formation depth of a given deformation mechanism and related diagenetic process.
3) The established gradual shift in oxygen and carbon isotopes with time reflects both the increase in fluid temperature and the proportion of meteoric water in the percolating fluids. This is due to continuous subsidence, increasing heat flow during rifting, and the enlargement of fluid-flow cells. This trend in the isotopes was not dramatically modified by the switch in tectonic settings from pre-rift compression-transpression to synrift extension.
4) Cement precipitation shows a spatial variation and it can be tied to the most active pre- and *syn*-rift deformation phases which resulted in rapid subsidence along the burial path. No calcite-cemented deformation structures were formed during the post-rift or neotectonic phases.
5) The existence of a basin-wide trend in isotopic values reveals a deviating, local contribution of a fluid enriched in light carbon isotope to the regional paleo-fluid-flow system. In addition, their connection to distinct deformation elements confirms the timing of this local contribution.
6) The different types of structures reveal variable characteristics in preserving the signals of the diagenetic process (calcite cementation). Calcite cement in disaggregation bands and host rock shows overlapping oxygen and carbon isotopic signatures. Therefore their cementation could be at least partly simultaneous processes as a result of comparable fluid-flow conductivity properties.
7) Protocataclastic bands strongly favoured calcite precipitation, in which enhanced fluid flow along the porosity contrast between the band core and margin may have played important role.
8) The δ^{18}OPDB and $\delta^{13}C_{PDB}$ isotopic signals of calcite in protocataclastic bands deviate from those in host rock's. Accordingly, this band type is capable of recording a distinct stage of diagenetic alteration, referring to the paleo fluid-flow system which reigned at very shallow burial conditions (<1 km).
9) All calcite veins preserved different δ^{18}OPDB and $\delta^{13}C_{PDB}$ isotopic values compared to the adjacent host rock and have constant $\delta^{13}C_{PDB}$ isotope values.
10) Coeval formation of the advanced stage of cataclastic bands and veins suggest inhomogeneous cementation of the host rock that influenced the mode of failure at the time of deformation.

Declaration of Competing Interest

The authors declare that they have no known competing financial interests or personal relationships that could have appeared to influence the work reported in this paper.

Acknowledgments

The research was supported by Hungarian Scientific Research Fund (NKFIH OTKA) 83150 and 113013. The stable isotope measurements were supported through the New National Excellence Program of the 699 Ministry of Human Capacities, Hungary (ÚNKP-17). The help and suggestions of Attila Balázs (ETH Zürich, Switzerland) for subsidence curve construction and heat flow history are acknowledged here. The detailed comments and suggestions of the reviewers (Sadoon Morad and an anonymous one) largely improved the initial manuscript.

References

Abreu, V.S., Haddad, G.A., 1998. Glacioeustatic fluctuations: the mechanism linking stable isotope events and sequence stratigraphy from the early Oligocene to Middle Miocene. SEPM Spec. Publ. 60, 245–259.
Andre, G., Hibsch, C., Fourcade, S., Cathelineau, M., Buschaert, S., 2010. Chronology of fracture sealing under a meteoric fluid environment: Microtectonic and isotopic evidence of major Cainozoic events in the eastern Paris Basin (France). Tectonophysics 490 (3), 214–228.
Antonellini, M.A., Aydin, A., 1994. Effect of faulting on fluid-flow in porous sandstones – Petrophysical properties. Am. Assoc. Pet. Geol. Bull. 78, 355–377.
Arató, R., Dunkl, I., Takács, Á., Szebényi, G., Gerdes, A., von Eynatten, H., 2019. Thermal evolution in the exhumed basement of a stratovolcano: case study of the Miocene Mátra Volcano, Pannonian Basin. J. Geol. Soc. 175 (5), 820–835.
Aydin, A., 1978. Small faults formed as deformation bands in sandstone. Pure Appl. Geophys. 116, 913–930.
Aydin, A., Johnson, A.M., 1978. Development of faults as zones of deformation bands and as slip surfaces in sandstones. — Pure Appl. Geophys. 116, 931–942.
Balázs, A., Matenco, L., Magyar, I., Horváth, F., Cloetingh, S., 2016. The link between tectonics and sedimentation in back-arc basins: new genetic constraints from the analysis of the Pannonian Basin. Tectonics 35, 1526–1559. https://doi.org/10.1002/2015TC004109.
Báldi, T., 1986. Mid-Tertiary Stratigraphy and Paleogeographic Evolution of Hungary. Akadémiai Kiadó, Budapest.
Ballas, G., Soliva, R., Sizun, J.-P., Benedicto, A., Cavailhes, T., Raynaud, S., 2012. The importance of the degree of cataclasis in shear bands for fluid flow in porous sandstone (Provence, FRANCE). Am. Assoc. Pet. Geol. Bull. 96, 2167–2186.
Ballas, G., Soliva, R., Benedicto, A., Sizun, J.P., 2014. Control of tectonic setting and large-scale faults on the basin-scale distribution of deformation bands in porous sandstone (Provence, France). Mar. Pet. Geol. 55, 142–159.
Balsamo, F., Storti, F., Gröcke, D.R., 2012. Fault-related fluid flow history in shallow marine sediments from carbonate concretions, Crotone basin, South Italy. J. Geol. Soc. London 169 (5), 613–626.
Banner, J.L., Hanson, G.N., 1990. Calculation of simultaneous isotopic and trace element variations during water-rock interaction with applications to carbonate diagenesis. Geochim. Cosmochim. Acta 54, 3123–3137.
Beaudoin, N., Bellahsen, N., Lacombe, O., Emmanuel, L., Pironon, J., 2014. Crustal-scale fluid flow during the tectonic evolution of the Bighorn Basin (Wyoming, USA). Basin Res. 26, 403–405.
Beitler, B., Parry, W.T., Chan, M.A., 2005. Fingerprints of fluid flow: chemical diagenetic history of the Jurassic Navajo Sandstone, Southern Utah, U.S.a. J. Sediment. Res. 75, 547–561.
Beke, B., Fodor, L., Millar, L., Petrik, A., 2019. Deformation band formation as a function of progressive burial: depth calibration and mechanism change in the Pannonian Basin (Hungary). Mar. Pet. Geol. 105, 1–16.
Bertotti, G., de Graaf, S., Bisdom, K., Oskam, B., Vonhof, H.B., Bezerra, F.H.R., Reijmer, J.J.G., Cazarin, C.L., 2017. Fracturing and fluid-flow during post-rift subsidence in carbonates of the Jandaira Formation, Potiguar Basin, NE Brazil. Basin Res. 29 (6), 836–853. https://doi.org/10.1111/bre.12246.
Bjørlykke, K., Egeberg, K., 1993. Quartz cementation in sedimentary basins. Am. Ass. Petr. Geol. Bull. 77, 1538–1548.
Boles, J.R., Eichhubl, P., Garven, G., Chen, J., 2004. Evolution of a hydrocarbon migration pathway along basin bounding faults: Evidence from fault cement. Am. Assoc. Pet. Geol. Bull. 88 (7), 947–970. https://doi.org/10.1306/02090403040.
Chan, M.A., Parry, W.T., Bowman, J.R., 2000. Diagenetic hematite and manganese oxides and fault-related fluid flow in Jurassic sandstones, southern Utah. Am. Assoc. Pet. Geol. Bull. 84, 1281–1310.
Csontos, L., Nagymarosy, A., 1998. The Mid-Hungarian line: a zone of repeated tectonic inversions. Tectonophysics 297, 51–71.
Davatzes, N.C., Aydin, A., Eichhubl, P., 2003. Overprinting faulting mechanisms during the development of multiple fault sets in sandstone, Chimney Rock fault array, Utah, U.S.a. Tectonophysics 363 (1–2), 1–18.

De Boever, E., Muchez, P., Swennen, R., Dimitrov, L., 2011. Evolution of deformation and fault-related fluid flow within an ancient methane seep system (Eocene, Varna, Bulgaria). Geofluids 11, 166–183. https://doi.org/10.1111/j.1468-8123.2011.00328.x.

de Graaf, S., Reijmer, J.J.G., Bertotti, G.V., Bezerra, F.H.R., Cazarin, C.L., Bisdom, K., Vonhof, H.B., 2017. Fracturing and calcite cementation controlling fluid flow in the shallow-water carbonates of the Jandaíra Formation. Brazil. Mar. Pet. Geol. 80, 382–393.

Del Sole, L., Antonellini, M., 2019. Microstructural, petrophysical, and mechanical properties of compactive shear bands associated to calcite cement concretions in arkose sandstone. J. Struct. Geol. 126, 51–68.

Dickson, J., 1966. Carbonate identification and genesis as revealed by staining. J. Sediment. Petrol. 36, 491–505.

Eichhubl, P., Taylor, W.L., Pollard, D.D., Aydin, A., 2004. Paleo-fluid flow and deformation in the Aztec Sandstone at the Valley of Fire, Nevada—evidence for the coupling of hydrogeologic, diagenetic, and tectonic processes. Geol. Soc. Am. Bull. 116, 1120–1136.

Eichhubl, P., Davatzes, N.C., Becker, S.P., 2009. Structural and diagenetic control of fluid migration and cementation along the Moab fault. Utah. Am. Assoc. Petr. Geol. Bull. 93, 653–681.

Ferrill, A.D., Morris, A.P., 2003. Dilational normal faults. J. Struct. Geol. 25, 183–196.

Fodor, L., Csontos, L., Bada, G., Györfi, I., Benkovics, L., 1999. Tertiary tectonic evolution of the Pannonian basin system and neighbouring orogens: a new synthesis of paleostress data. In: Durand, B., Jolivet, L., Horváth, F., Séranne, M. (Eds.), The Mediterranean Basins: Tertiary extension within the Alpine Orogen. Geological Society, 156. Special Publications, London, pp. 295–334.

Fodor, L., Radócz, Gy, Sztanó, O., Koroknai, B., Csontos, L., Harangi, Sz, 2005. Postconference excursion: tectonics, sedimentation and magmatism along the Darnó zone. Geolines 19, 142–162.

Folk, R.L., 1974. Petrology of Sedimentary Rocks Austin. Hemphill Publishing Company, Texas.

Fossen, H., Schultz, R., Shipton, Z., Mair, K., 2007. Deformation bands in sandstone – a review. J. Geol. Soc. Lond. 164, 755–769.

Fossen, H., Soliva, R., Ballas, G., Trzaskos, B., Cavalcante, G.C., Schultz, R.A., 2017. A review of deformation bands in reservoir sandstones: geometries, mechanisms and distribution. Geol. Soc. Special Paper 459, 9–33.

Goldstein, R.H., Reynolds, T.J., 1994. Systematics of Fluid Inclusions in Diagenetic Minerals. In: SEPM Society for Sedimentary Geology, 31. SEPM Short Course Notes.

Hámor, G., 1985. Geology of the Nógrád–Cserhát area. Geol. Hungarica Series Geol. 22, 1–307.

Havril, T., Molson, J.R., Mádl-Szőnyi, J., 2016. Evolution of fluid flow and heat distribution over geological time scales at the margin of unconfined and confined carbonate sequences - a numerical investigation based on the Buda thermal Karst analogue. Mar. Pet. Geol. 78, 738–749.

Hodson, K.R., Crider, J.G., Huntington, K.W., 2016. Temperature and composition of carbonate cements record early structural control on cementation in a nascent deformation band fault zone: Moab Fault, Utah, USA. Tectonophysics 690, 240–252.

Hohenegger, J., Ćorić, S., Wagreich, M., 2014. Timing of the middle Miocene Badenian stage of the central Paratethys. Geol. Carpath. 65, 55–66.

Horváth, F., Musitz, B., Balázs, A., Végh, A., Uhrin, A., Nádor, A., Koroknai, B., Pap, N., Tóth, T., Wórum, G., 2015. Evolution of the Pannonian basin and its geothermal resources. Geothermics 53, 328–352.

Kim, S.T., O'Neil, J.R., 1997. Equilibrium and nonequilibrium oxygen isotope effects in synthetic carbonates. Geochim. Cosmochim. Acta 61, 3461–3475.

Knipe, R.J., 1993. The influence of fault zone processes and diagenesis on fluid flow. In: Horbury, A.D., Robinson, A.G. (Eds.), Diagenesis and Basin Development. Am. Assoc. Petr. Geol. Studies in Geology, 36, pp. 135–154.

Kováč, M., Halásová, E., Hudáčková, N., Holcová, K., Hyžný, M., Jamrich, M., Ruman, A., 2018. Towards better correlation of the Central Paratethys regional time scale with the standard geological time scale of the Miocene Epoch. Geol. Carpathica 69 (/3), 283–300. https://doi.org/10.1515/geoca-2018-0017.

Kovács, S., Ozsvárt, P., Palinkaš, L., Kiss, G., Molnár, F., Józsa, S., Kövér, Sz, 2010. Re-evaluation of the Mesozoic of the Darnó Hill (NE Hungary) and comparison with Neotethyan accretionary complexes of the Dinarides and Hellenides - preliminary data. Cent. Eur. Geol. 53 (2–3), 205–231.

Kovács, Zs, Cserkész-Nagy, Á., Gulyás, Á., Gúthy, T., Kiss, J., Püspöki, Z., Szentpétery, I., Szalay, I., 2020. Mapping of the Salgótarján and Ózd Palaeogene subbasins based on seismic and gravity measurement data, and its hydrocarbon geological aspects. Földtani Közlöny 150 (1), 103–128. https://doi.org/10.23928/foldt.kozl.2020.150.1.103.

Laubach, S.E., Eichhubl, P., Hilgers, C., Lander, R.H., 2010. Structural diagenesis. J. Struct. Geol. 32 (12), 1866–1872.

Less, Gy, Frijia, G., 2015. New Sr-isotope ages from the Central Parathetys. In: Hungarian Paleontological Assembly, 18th. Field Guide, Budapest, pp. 19–20.

Lohmann, K., 1988. Geochemical patterns of meteoric diagenetic systems and their application to studies of paleokarst. In: James, N.P., Choquette, P.W. (Eds.), Paleokarst. Springer-Verlag, New York, pp. 58–80.

Lommatzsch, M., Exner, U., Gier, S., Grasemann, B., 2015a. Structural and chemical controls of deformation bands on fluid flow: interplay between cataclasis and diagenetic alteration. Am. Assoc. Pet. Geol. Bull. 99 (4), 698–710. https://doi.org/10.1306/10081413162.

Lommatzsch, M., Exner, U., Gier, S., Grasemann, B., 2015b. Dilatant shear band formation and diagenesis in calcareous, arkosic sandstones, Vienna Basin (Austria). Mar. Pet. Geol. 62, 144–160.

Lukács, R., Harangi, S., Guillong, M., Bachmann, O., Fodor, L., Buret, Y., Dunkl, I., Sliwinski, J., von Quadt, A., Peytcheva, I., Zimmerer, M., 2018. Early to Mid-Miocene syn-extensional massive silicic volcanism in the Pannonian Basin (East-Central Europe): Eruption chronology, correlation potential and geodynamic implications. Earth-Sci. Rev. 179, 1–19.

Mangenot, X., Gasparrini, M., Rouchon, V., Bonifacie, M., 2018. Basin scale thermal and fluid-flow histories revealed by carbonate clumped isotopes (Δ47) - Middle Jurassic carbonates of the Paris Basin depocentre. Sedimentology 65 (1), 1–29.

Márton, E., Fodor, L., 1995. Combination of paleomagnetic and stress data — a case study from North Hungary. Tectonophysics 242, 99–114.

McBride, E.F., 1989. Quartz cement in sandstones: a review. Earth-Sci. Rev. 26, 69–112.

McRea, M., 1950. The isotopic chemistry of carbonates and a paleotemperature scale. J. Chem. Phys. 18, 849–857.

Milliken, K.L., McBride, E.F., Cavazza, W., Cibin, U., Fontana, D., Picard, M.D., Zuffa, G. G., 2009. Geochemical history of Calcite Precipitation in Tertiary Sandstones, Northern Apennines, Italy. In: Morad, S. (Ed.), Carbonate Cementation in Sandstones. https://doi.org/10.1002/9781444304893.ch10.

Morad, S., Ketzer, J.M., De Ros, L.F., 2000. Spatial and temporal distribution of diagenetic alterations in siliciclastic rocks: implications for mass transfer in sedimentary basins. Sedimentology 47, 95–120.

Mozley, P.S., Goodwin, L.B., 1995. Patterns of cementation along a Cenozoic normal fault: a record of paleoflow orientations. Geology 23, 539–542.

Ogata, K., Senger, K., Braathen, A., Tveranger, J., 2014. Fracture corridors as seal-bypass systems in siliciclastic reservoir-cap rock successions: Field-based insights from the Jurassic Entrada Formation (SE Utah, USA). J. Struct. Geol. 66, 162–187.

Palotai, M., Csontos, L., 2010. Strike-slip reactivation of a Palaeogene to Miocene fold and thrust belt along the central part of the Mid-Hungarian Shear Zone. Geol. Carpath. 61 (6), 483–493.

Petrik, A., Beke, B., Fodor, L., 2014. Combined analysis of faults and deformation bands reveals the Cenozoic structural evolution of the southern Bükk foreland (Hungary). Tectonophysics 633, 43–62.

Petrik, A., Beke, B., Fodor, L., Lukács, R., 2016. Cenozoic structural evolution of the southwestern Bükk Mts. And the southern part of the Darnó Deformation Belt (NE Hungary) Geol. Carpathica 67, 83–104.

Pittman, E.D., 1981. Effect of fault-related granulation on porosity and permeability of quartz sandstones, Simpson Group (Ordovician) Oklahoma. Am. Assoc. Pet. Geol. Bull. 65, 2381–2387.

Rotevatn, A., Sandve, T.H., Keilegavlen, E., Kolyukhin, D., Fossen, H., 2013. Deformation bands and their impact on fluid flow in sandstone reservoirs: the role of natural thickness variations. Geofluids 13, 359–371.

Saigal, G.C., Morad, S., Bjorlykke, K., Egeberg, P.K., Aagaard, P., 1988. Diagenetic albitization of detrital K-feldspar in Jurassic, lower cretaceous, and Tertiary clastic reservoir rocks from offshore Norway; I, Textures and origin. J. Sediment. Res. 58 (6), 1003–1013.

Sant, K., Palcu, D.V., Mandic, O., Krijgsman, W., 2017. Changing seas in the Early–Middle Miocene of Central Europe: a Mediterranean approach to Paratethyan stratigraphy. Terra Nova 29, 273–281. https://doi.org/10.1111/ter.12273.

Schultz, R.A., Siddharthan, R., 2005. A general framework for the occurrence and faulting of deformation bands in porous granular rocks. Tectonophysics 411, 1–18.

Shipton, Z.K., Evans, J.P., Thompson, L.B., 2005. The geometry and thickness of deformation band fault core and its influence on sealing characteristics of deformation band fault zones. In: Sorkhabi, R., Tsuji, Y. (Eds.), Fault, Fluid Flow and Petroleum Traps, Am. Assoc. Petr. Geol. Memoir, vol. 85, pp. 181–195.

Sigda, J.M., Goodwin, L.B., Mozley, P.S., Wilson, J.L., 1999. Permeability alteration in small-displacement faults in poorly lithified sediments: Rio Grande Rift, Central New Mexico. In: Haneberg, W.C., Mozley, P.S., Moore, C.J., Goodwin, L.B. (Eds.), Faults and Subsurface Fluid Flow. Geoph. Monograph, 113. Am. Geoph. Union, pp. 51–68.

Skurtveit, E., Torabi, A., Alikarami, R., Braathen, A., 2015. Fault baffle to conduit developments: reactivation and calcite cementation of deformation band fault in aeolian sandstone. Pet. Geosci. 21, 3–16.

Soliva, R., Ballas, G., Fossen, H., Philit, S., 2016. Tectonic regime controls clustering of deformation bands in porous sandstone. Geology 44 (6), 423–426.

Szőcs, E., Hips, K., 2018. Multiphase carbonate cementation in the Miocene Pétervására Sandstone (North Hungary): implications for basinal fluid flow and burial history. Geol. Carpathica 69 (6), 515–527.

Sztanó, O., 1994. The tide-influenced Pétervására Sandstone, early Miocene, northern Hungary: Sedimentology, paleogeography and basin development. Geol. Ultraiect. 120, 1–155.

Sztanó, O., 1995. Palaeogeographic significance of tidal deposits: an example from an early Miocene Paratethys embayment, Northern Hungary. Palaeogeogr. Palaeoclimatol. Palaeoecol. 113 (2), 173–187.

Sztanó, O., Józsa, S., 1996. Interaction of basin-margin faults and tidal currents on nearshore sedimentary architecture and composition: a case study from the early Miocene of northern Hungary. Tectonophysics 266 (1), 319–341.

Sztanó, O., Tari, G., 1993. Early Miocene basin evolution in northern Hungary: tectonics and eustasy. Tectonophysics 226 (1), 485–502.

Tari, G., Báldi, T., Báldi-Beke, M., 1993. Paleogene retroarc flexural basin beneath the Neogene Pannonian Basin: a geodynamic model. Tectonophysics 226, 433–455.

Torabi, A., Fossen, H., 2009. Spatial variation of microstructure and petrophysical properties along deformation bands in reservoir sandstones. Am. Assoc. Pet. Geol. Bull. 93, 919–938.

Torabi, A., Fossen, H., Braathen, A., 2013. Insight into petrophysical properties of deformed sandstone reservoirs. Am. Assoc. Pet. Geol. Bull. 97, 619–637.

Travé, A., Calvet, F., Soler, A., Labaume, P., 1998. Fracturing and fluid migration during Palaeogene compression and Neogene extension in the Catalan Coastal Ranges, Spain. Sedimentology 45 (6), 1063–1082.

Tueckmantel, C., Fisher, Q.J., Grattoni, C.A., Aplin, A.C., 2012. Single-and two-phase fluid flow properties of cataclastic fault rocks in porous sandstone. Mar. Pet. Geol. 29, 129–142.

van Balen, R.T., Cloetingh, S.A.P.L., 1993. Stress-induced fluid flow in rifted basins. In: Horbury, A.D., Robinson, A.G. (Eds.), Diagenesis and Basin development, American Assoc. of Petr. Geologists Studies in Geology, pp. 87–98.

Vass, D., Kováč, M., Konecny, V., Lexa, J., 1988. Molasse basins and volcanic activity in the West Carpathian Neogene: its evolution and geodynamic character. Geol. Carpath. 39, 539–561.

Virág, M., 2018. Hypogene and epigene karstic processes and their influence on the evolution of the Rózsadomb caves in Buda – by the example of Szemlő-hegy Cave and Molnár János Cave. Ph.D. thesis. Eötvös Loránd University, Budapest, p. 318.

Williams, R.T., Goodwin, L.B., Mozley, P.S., 2017. Diagenetic controls on the evolution of fault-zone architecture and permeability structure: Implications for episodicity of fault-zone fluid transport in extensional basins. Geol. Soc. Am. Bull. 129 (3–4), 464–478. https://doi.org/10.1130/B31443.1.

Wilson, J.E., Goodwin, L.B., Lewis, C., 2006. Diagenesis of deformation band faults: Record and mechanical consequences of vadose zone flow and transport in the Bandelier Tuff, Los Alamos, New Mexico. J. Geophys. Res. 111, B09201 https://doi.org/10.1029/2005JB003892.

Zelenka, T., Baksa, Cs, Balla, Z., Földessy, J., Földessy-Járányi, K., 1983. The role of the Darnó Line in the basement structure of Northeast Hungary. Geologický Zborník Geologica Carpathica 34, 53–69.